PHYSICS OF FLUIDS - Accepted November 24th 2022

Comparative heat transfer analysis of electroconductive $Fe_3O_4-MWCNT-$water and $Fe_3O_4-MWCNT-$kerosene hybrid nanofluids in a square porous cavity using the non-Fourier heat flux model

Thirumalaisamy K,[1, a)] Sivaraj Ramachandran,[1] Sivaraj Ramachandran,[b)] Ramachandra Prasad V,[a)] Anwar Bég O,[c)] Ho-Hon Leung,[b)] Firuz Kamalov,[d)] and Panneer Selvam R[e)]

Department of Mathematics, School of Advanced Sciences, Vellore Institute of Technology, Vellore 632014, India.

(*Electronic mail: sivaraj.kpm@gmail.com)

(Dated: 10 November 2022)

The analysis on heat transmission and fluid flow characteristics within the cavity is useful to improve the features of several applications including energy storage devices and hybrid fuel cells. With this motivation, the present model investigates the characteristics of magneto-convective heat transmission and fluid flow within a square porous enclosure with hot and cold slits. The heat transfer features of electrically conducting hybrid nanofluids $Fe_3O_4-MWCNT-$water and $Fe_3O_4-MWCNT-$kerosene is analyzed inside the enclosure. The non-Fourier thermal flux model is deployed and the internal heat absorption/generation effect is considered. The Marker-And-Cell (MAC) numerical scheme is adopted to solve the transformed dimensionless mathematical model with associated initial-boundary conditions. An exhaustive parametric investigation is implemented to estimate the influence of key parameters on the transport phenomena. The computations show that augmenting the Hartmann number values modify the fluid flow and temperature features substantially for both the hybrid nanofluids. Enhancing the values of nanoparticles volume fraction promotes the heat transfer. When 5% $Fe_3O_4-MWCNT$ nanoparticles are suspended into water and kerosene base fluids, $Fe_3O_4-MWCNT-$kerosene hybrid nanofluid achieves 6.85% higher mean heat transfer rate compared to $Fe_3O_4-MWCNT-$water hybrid nanoliquid. In the existence of heat absorption, the mean rate of heat transfer of $Fe_3O_4-MWCNT-$water hybrid nanofluid is 78.92% lower than $Fe_3O_4-MWCNT-$kerosene hybrid nanoliquid. Greater energy transmission is noticed in the case of $Fe_3O_4-MWCNT-$kerosene hybrid nanofluid and the enhanced fluid flow is noticed in the case of $Fe_3O_4-MWCNT-$water hybrid nanofluid. Fourier's model ($\delta_e = 0$) estimates higher heat transfer rate than that of the Cattaneo–Christov (non-Fourier) heat flux model ($\delta_e \neq 0$).

Keywords: Magnetized hybrid nanofluids, square cavity, Cattaneo Christov heat flux, MAC computation, heat source/sink.

I. INTRODUCTION

Mixed convection arises in a variety of thermal engineering applications wherein energy transfer occurs without the presence of any external forces. The vital engineering applications of mixed convection include in nuclear reaction systems, air-condition refrigerators, cooling of electronic devices, solar collectors, and heat exchangers. As a result, numerous researchers scrutinized the features of mixed convective flow and heat transmission inside the cavities by employing various theoretical techniques[1,2]. In the current era, due to several practical applications, natural and mixed convective flows are investigated inside different types of geometries, for example, tilted cavity, annular cavity, open cavity, square, L-shape, rectangular, triangular, and trapezoidal enclosures[3–10]. Convective flow and heat transmission in such cavities features in diverse engineering systems including room ventilation, nuclear and chemical reactors, geothermal systems, drying devices, fuel cells, fire dynamics in compartments, food processing, and thermal energy storage systems[11].

The thermophysical properties of ordinary fluids, such as thermal conductivity may be enhanced by adding nanoparticles into base fluids. In numerous practical applications, including petroleum recovery, heat pipes, chemical processes, lubrication, surface coating, heat exchangers, biomedical systems, environmental remediation, and electronic cooling systems due to their enhanced thermal efficiency[12–16]. Nanofluids are prepared by suspending the nano-sized $(1-100nm)$ particles into a base fluid. The nanoparticles are synthesized from metals $(Cu, Ag, Al, \& Au)$, metal$-$oxides $(Fe_2O_3, SiO_2, ZnO, TiO_2, Al_2O_3, CuO, CuO_2, Fe_3O_4)$, carbon-based (MWCNTs, SWCNTs, & carbon nanotubes), and metal nitride (AlN)[17–19]. These metallic/non$-$metallic nanoparticles are carefully suspended into the ethylene glycol/water/propylene glycol/kerosene/ oil or other base fluids, to augment the base fluid's thermal conductivity. It is to be noted that metallic nanoparticles like Al, Cu, Au, Ag, Fe, Zn and Ni are recognized for their excellent thermal conductivity.

[a)]Department of Mathematics, School of Advanced Sciences, Vellore Institute of Technology, Vellore 632014, India.
[b)]Department of Mathematical Sciences, United Arab Emirates University, Al Ain, United Arab Emirates.
[c)]Multi-Physical Engineering Sciences Group (MPESG), Aeronautical and Mechanical Engineering Department, School of Science, Engineering and Environment, University of Salford, Manchester M54WT, UK.
[d)]Faculty of Engineering, Canadian University Dubai, Dubai, United Arab Emirates.
[e)]Department of Civil Engineering, BELL 4190 University of Arkansas, Fayetteville, AR 72701, USA.

Although silver and gold nanoparticles feature very high thermal conductivities, relatively sparse investigations have been conducted because of the high cost of these precious metals. Accordingly, adding the metallic oxide nanoparticles, which are less costly, may have a favorable influence on the production of more efficacious nanofluids in terms of economical optimization in addition to the stability and thermal performance[20,21]. However, preparing the nanofluids by using a single type of nanoparticles (unitary nanofluids) has shown its limitations and deficiencies. Therefore, researchers have developed the hybrid nanofluids by combining more than one type of nanoparticles with base-fluids. This concept has been revealed as an innovative approach to enhance the energy transmission in various devices, notably in fuel cells. However, it is critical to judiciously select appropriate and compatible types of nanoparticles. Many researchers have shown numerically and experimentally that hybrid nanofluids consistently produce a high heat transfer rate and greater thermal efficiency compared to ordinary fluids or unitary nanofluids[22,23]. Currently, the hybrid nanofluids are being explored in a wide spectrum of emerging technologies including heat pipes, cooling techniques in nuclear power systems, generators, transformers, thermal barrier coatings, automotive radiators, braking systems, electronic devices, and manufacturing. Further applications can be found in biomedical drug delivery, air conditioning, sensor surface finishing, etc[24,25].

Convective flow in porous media plays a major role in the design of chemical catalytic reactors, ground-water flows, fuel cells, heat exchangers, boilers, fluidized beds, cutting-edge innovation, tertiary recovery, chemical separations, the technology of porous ceramic burners, underground feeder cables, water filtration, drug transfer in tissues, thermal insulation, packed-bed energy storage systems, oil and gas flowing in reservoirs[26–30]. Darcy's law is the most popular model for simulating fluid motion in a porous medium. Non-Darcy phenomena are essential for understanding the fluid flow in porous media whenever high velocity is involved i.e. when inertial effects arise. Computational studies deal with the transport in non-Darcian porous medium have stimulated substantial attention by virtue of the ever-growing applications of this field in the twenty-first century. These studies have been examined by using several Newtonian liquids, non-Newtonian liquids, and nanofluids. Mythili et al.[31] presented a mathematical model to explore features of the chemically reactive Casson liquid flow over a plate and cone with the consequence of heat absorption/generation. They noticed that the fluid flow diminishes for augmenting the Casson parameter and Forchheimer number (non-Darcian quadratic drag). Alsabery et al.[32] scrutinized the free convective flow within a porous enclosure of square-shape filled with Al_2O_3-water nanofluid by considering the Brinkman-Forchheimer-extended Darcy model. They concluded that greater porosity of the medium enhances the average Nusselt number. Zehba et al.[33] examined the natural convective Al_2O_3-water nanofluid flow within a V-shaped enclosure containing a heterogeneous porous medium. They detected that higher Darcy number values improve the temperature gradients around the heated areas and hence increase the average Nusselt number. Shirani and Toghraie[34] numerically analyzed the mixed convective *Cu*-water nanoliquid flow within a porous cavity with the Forchheimer–Brinkman-extended Darcy model. They determined that with a decrement in Darcy parameter, the Nusselt number rises.

Magnetohydrodynamics (MHD) is the science of the interaction of electro-conductive fluids and magnetic fields. When an electro-conductive fluid crosses a magnetic field flux, an external body force known as the Lorentzian force is generated and this force acts against the fluid flow. Furthermore, the flow may induce magnetic field fluxes[35]. MHD is central to the design of new emerging hybrid electromagnetic fuel cells which are motivated by green, sustainable initiatives. It is a clean technology and circumvents the need for conventional combustion systems in power generation which are ecologically unfriendly. In parallel with laboratory testing of new magnetic fuel cells, numerical simulation of these devices is extremely beneficial for optimizing efficiency and predicting long-term performance. Muthtamilselvan and Doh[36] numerically investigated the mixed convective flow and energy transmission features of different nanofluids within an enclosure with the influence of a magnetic force by adopting a control volume technique. They discovered that the various types of nanofluid flow and energy transmission within the enclosures are highly reliant on the Hartmann and Reynolds numbers. Rashad et al.[37] theoretically scrutinized the MHD free convection flow of a hybrid nanofluid inside an enclosure of triangular-shape by adopting the finite difference method. They found that higher magnetic parameter values cause an augmentation in the Nusselt number. Du et al.[38] utilized the finite difference scheme to explore the MHD free convective $Al_2O_3 - Cu$-water hybrid nanofluid flow in an enclosure and noticed that an increase in magnetic parameter suppresses the effects of thermal buoyancy. Sowmya et al.[39] studied the free convective $Fe_3O_4 - Ag$-water hybrid nanofluid flow and energy transmission characteristics in heated fins attached rectangular enclosure through numerical simulations. They discovered that with high values of the Hartmann number and low values of the Rayleigh number, the flow appears to be laminar. However, at low values of the Hartmann number and high values of the Rayleigh number, they observed the onset of turbulent flow characteristics.

Heat generation or absorption plays an extremely influential role in different phenomena such as high-temperature fuel cell design. For the past few decades, many researchers have been contributing to improve the energy transfers features of nanoliquids inside various cavities. Teamah and Wael[40] numerically scrutinized the free convection flow within a square enclosure with various nanofluids under the impact of uniform heat absorption or generation by utilizing the finite volume method. They demonstrated that the energy transmission is enriched for magnifying the volume fraction values when the heat absorption parameter is frozen with the smaller values. Mliki et al.[41] examined the MHD free convective flow of copper-water nanoliquid within the cavity. They noticed that strengthening the heat generation parameter enhances the energy transmission. Hussain et al.[42] analyzed the thermal

performance of alumina-water nanofluid inside an enclosure under the impact of internal heat absorption or generation by employing the finite element technique. They noticed that the energy transmission and fluid flow are significantly modified with the variations in internal heat absorption or generation parameter. Abdulkadhim et al.[43] numerically explored the natural convective flow of copper-water nanoliquid inside a cavity containing a circular hot cylinder by adopting the Galerkin-weighted residual method.

Most of the studies generally considered the classical Fourier heat flux model. This model has a parabolic formulation for heat conduction and neglects thermal relaxation effects. To accommodate the relaxation rate of the heat flux, the Cattaneo-Christov heat flux model is required which is the non-Fourier hyperbolic conduction model featuring Oldroyd's upper-convected derivative in the Maxwell–Cattaneo equation. In addition, this type of formulation permits the elimination of heat flux by inducing a single equation for the temperature field as performed by Christov[44]. Muhammad et al.[45] deployed the Cattaneo–Christov heat flux model to numerically explore the transport phenomena of mixed convective Ag–ethylene glycol nanoliquid flow inside an enclosure. They exposed that compared to non-Fourier's heat flux model, the rate of heat transfer is higher in the case of Fourier's heat flux model. Jakeer et al.[46] investigated the convective flow characteristics of a hybrid nanoliquid inside an enclosure by using the Cattaneo-Christov heat flux model in the energy equation. Sivasankaran et al.[47] numerically explored the features of convective flow inside an enclosure of square-shape with the Cattaneo-Christov heat flux model. Garia et al.[48] numerically examined the MHD convective $SiO_2 - MoS_2$-water hybrid nanoliquid flow external to cone and wedge geometries with a generalized Cattaneo-Christov heat flux model. They determined that the Fourier's heat flux model estimates higher temperatures than the non-Fourier heat flux model.

To the best of the authors' knowledge, no analysis has been communicated so far to numerically examine the mixed convective energy transmission and flow features of a $Fe_3O_4 - MWCNT-$water and $Fe_3O_4 - MWCNT-$kerosene hybrid nanoliquid within the porous enclosure under the impact of the magnetic field and heat source/sink by adopting the Cattaneo–Christov heat flux model. In practical applications, many factors can enhance the heat transfer. The combination of nanoparticles and base fluids plays a significant role in optimizing the energy transmission features. The novelty of this investigation is to compare and identify the optimum energy transmission and flow features of $Fe_3O_4 - MWCNT-$water and $Fe_3O_4 - MWCNT-$kerosene hybrid nanoliquids within the porous square enclosure. In this analysis, hot sources are considered in the middle of the vertical sidewalls, and cold sinks are considered in the middle of the horizontal sidewalls. The remaining sections of the cavity walls are considered as adiabatic. The Tiwari-Das nanofluid volume fraction model is utilized in this analysis. The non-dimensional governing equations are solved by utilizing the MAC technique[49,50], and the numerical outcomes for streamlines, isotherms, average and local Nusselt numbers are displayed graphically. Validations with previous study are incorporated. It is to be noted that the deployment of hybrid nanofluids is of immediate relevance to the next generation hybrid electromagnetic fuel cells and may be beneficial to cooling application in nuclear systems, generators, transformers, and electronic devices.

II. MATHEMATICAL FORMULATION

In this section, details are provided for the current mathematical model. Figure. 1 schematically represents the two-dimensional geometry that is to be examined. The MHD mixed convective flow in a square porous cavity saturated with electrically conducting hybrid nanofluids is studied, as a model of a hybrid electromagnetic fuel cell system. The horizontal and vertical walls have length (L). The center parts of the left and right walls are maintained at a high temperature, whereas the center portions of the top and bottom walls are kept at a low temperature. Unsteady, laminar flow of incompressible fluids is considered. The square enclosure includes an isotropic, homogenous, non-deformable porous medium, and non-Darcy behavior is considered. Hybrid nanofluid's thermophysical properties are considered appropriate to the Tiwari-Das model. The flow domain is influenced by a static horizontal externally imposed magnetic field. The influences of internal heat absorption or generation and the non-Fourier thermal relaxation (Cattaneo-Christov heat flux) are considered. The strength of the applied magnetic field is B_0 and it is considered as uniform. It is assumed that the electric field is zero since the ionized fluid's polarization effect is negligible and no external electric field is considered. When the induced electric field is negligible and external electric field is zero, the magnetic Reynolds number is very small. As a consequence, the influence of Hall effect and induced magnetic field are neglected. Further, the variation of thermophysical properties including the viscosity and electrical conductivity is neglected. Furthermore, the considered base fluids (water and kerosene) are Newtonian fluids with low viscosities and the fluids are finitely conducting. So, impact of the viscous dissipation, Joule heating and resistant heating term due to porous medium are neglected.

Based upon the above approximations, the mathematical model features the hybrid nanofluid expressions in the form of the conservation laws of mass, momentum, and energy[36,40,42,45,46,51]:

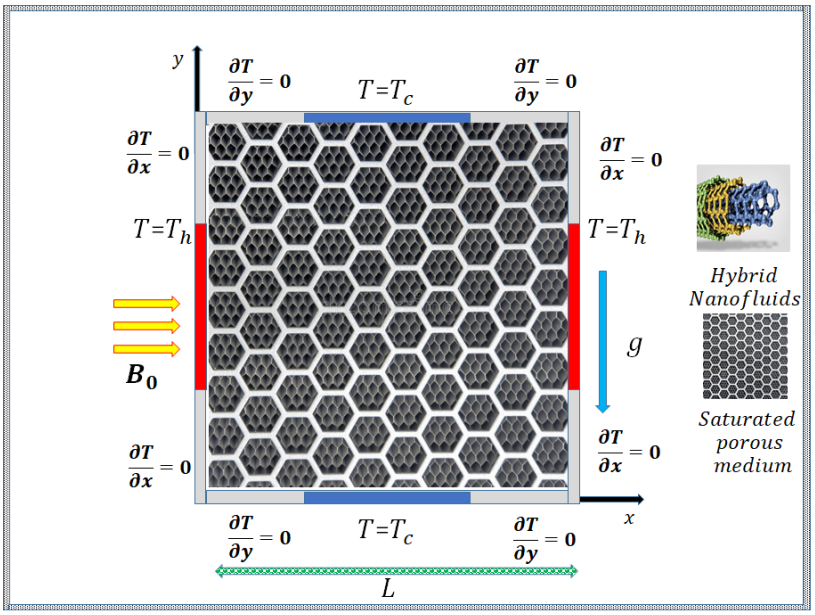

FIG. 1. Flow configuration of the problem.

$$\frac{\partial u}{\partial x}+\frac{\partial v}{\partial y}=0 \tag{1}$$

$$\frac{\partial u}{\partial t^*}+u\frac{\partial u}{\partial x}+v\frac{\partial u}{\partial y}=-\frac{1}{\rho_{hnf}}\frac{\partial p}{\partial x}+\nu_{hnf}\left[\frac{\partial^2 u}{\partial x^2}+\frac{\partial^2 u}{\partial y^2}\right] -\frac{\nu_{hnf}}{K}u-\frac{F}{\sqrt{K}}u\sqrt{u^2+v^2} \tag{2}$$

$$\frac{\partial v}{\partial t^*}+u\frac{\partial v}{\partial x}+v\frac{\partial v}{\partial y}=-\frac{1}{\rho_{hnf}}\frac{\partial p}{\partial y}+\nu_{hnf}\left[\frac{\partial^2 v}{\partial x^2}+\frac{\partial^2 v}{\partial y^2}\right] -\frac{\nu_{hnf}}{K}v-\frac{F}{\sqrt{K}}v\sqrt{u^2+v^2} +\frac{(\rho\beta)_{hnf}}{\rho_{hnf}}g(T-T_c)-\frac{\sigma_{hnf}B_0^2}{\rho_{hnf}}v \tag{3}$$

$$\frac{\partial T}{\partial t^*}+u\frac{\partial T}{\partial x}+v\frac{\partial T}{\partial y}=\frac{k_{hnf}}{(\rho C_p)_{hnf}}\left[\frac{\partial^2 T}{\partial x^2}+\frac{\partial^2 T}{\partial y^2}\right]+\frac{Q_0}{(\rho C_p)_{hnf}}(T-T_c) -\delta\left(u\frac{\partial u}{\partial x}\frac{\partial T}{\partial x}+v\frac{\partial v}{\partial y}\frac{\partial T}{\partial y}+u^2\frac{\partial^2 T}{\partial x^2}+v^2\frac{\partial^2 T}{\partial y^2}\right) -\delta\left(2uv\frac{\partial^2 T}{\partial x\partial y}+u\frac{\partial v}{\partial x}\frac{\partial T}{\partial y}+v\frac{\partial u}{\partial y}\frac{\partial T}{\partial x}\right) \tag{4}$$

The initial-boundary conditions imposed on the enclosure's walls are given in Table 1.

Hybrid nanofluid's thermophysical properties are necessary for enhancing the energy transfer. The mono and hybrid nanofluids thermophysical properties are assumed appropriate to the Tiwari-Das model and are represented as follows[52]:

Table 2 summarizes the thermophysical properties of the base fluids and nanoparticles[53,54].

The subsequent non-dimensional quantities are defined to simplify the equations (1)–(4) toward the non-dimensional form:

$$U=\frac{u}{U_0};V=\frac{v}{U_0};X=\frac{x}{L};Y=\frac{y}{L}; P=\frac{p}{\rho_{hnf}U_0^2};\theta=\frac{T-T_c}{T_h-T_c};t=\frac{t^*U_0}{L} \tag{5}$$

By virtue of Eqn. (5), the subsequent governing equations appear in the dimensionless form:

$$\frac{\partial U}{\partial X}+\frac{\partial V}{\partial Y}=0 \tag{6}$$

$$\frac{\partial U}{\partial t}+U\frac{\partial U}{\partial X}+V\frac{\partial U}{\partial Y}=-\frac{\partial P}{\partial X}+\left(\frac{\nu_{hnf}}{\nu_f}\right)\frac{1}{Re}\left[\frac{\partial^2 U}{\partial X^2}+\frac{\partial^2 U}{\partial Y^2}\right] -\left(\frac{\nu_{hnf}}{\nu_f}\right)\frac{1}{Re\,Da}U-\frac{F}{\sqrt{Da}}U\sqrt{U^2+V^2} \tag{7}$$

$$\frac{\partial V}{\partial t}+U\frac{\partial V}{\partial X}+V\frac{\partial V}{\partial Y}=-\frac{\partial P}{\partial Y}+\left(\frac{\nu_{hnf}}{\nu_f}\right)\frac{1}{Re}\left[\frac{\partial^2 V}{\partial X^2}+\frac{\partial^2 V}{\partial Y^2}\right] -\left(\frac{\nu_{hnf}}{\nu_f}\right)\frac{1}{Re\,Da}V-\frac{F}{\sqrt{Da}}V\sqrt{U^2+V^2}+\frac{(\rho\beta)_{hnf}}{\rho_{hnf}\beta_f}Ri\,\theta -\left(\frac{\rho_f}{\rho_{hnf}}\right)\left(\frac{\sigma_{hnf}}{\sigma_f}\right)\frac{Ha^2}{Re}V \tag{8}$$

$$\frac{\partial \theta}{\partial t}+U\frac{\partial \theta}{\partial X}+V\frac{\partial \theta}{\partial Y}=\left(\frac{\alpha_{hnf}}{\alpha_f}\right)\frac{1}{Re\,Pr}\left[\frac{\partial^2 \theta}{\partial X^2}+\frac{\partial^2 \theta}{\partial Y^2}\right] +\left(\frac{\alpha_{hnf}}{\alpha_f}\right)\frac{Q}{Re\,Pr}\theta-\delta_e\left(U\frac{\partial U}{\partial X}\frac{\partial \theta}{\partial X}+V\frac{\partial V}{\partial Y}\frac{\partial \theta}{\partial Y}+U^2\frac{\partial^2 \theta}{\partial X^2}+V^2\frac{\partial^2 \theta}{\partial Y^2}\right) -\delta_e\left(2UV\frac{\partial^2 \theta}{\partial X\partial Y}+U\frac{\partial V}{\partial X}\frac{\partial \theta}{\partial Y}+V\frac{\partial U}{\partial Y}\frac{\partial \theta}{\partial X}\right) \tag{9}$$

The relevant dimensionless parameters featured in Eqns. (7)-(9) are summarized in Table 3. The transformed dimensionless boundary conditions associated with Eqns. (6)-(9) are listed in Table 4.

Nusselt number: The local and mean Nusselt numbers (wall heat transfer rate) are given by the subsequent expressions:

$$Nu=-\frac{k_{hnf}}{k_f}\left(\frac{\partial \theta}{\partial Y}\right)_{Y=0} \tag{10}$$

$$Nu_{avg}=\int_0^1 Nu\,dX \tag{11}$$

TABLE I. The dimensional form of initial-boundary conditions[21,47].

Initial condition $t^* \leq 0$, $0 \leq x \leq L$, $0 \leq y \leq L$:	$u = v = 0$	$T = T_c$
Left wall $t^* > 0$, $x = 0$:	$u = v = 0$,	$\frac{\partial T}{\partial x} = 0$ for $0 \leq y \leq 0.25L$
	$0 \leq y \leq L$:	$T = T_h$ for $0.25L \leq y \leq 0.75L$
		$\frac{\partial T}{\partial x} = 0$ for $0.75L \leq y \leq L$
Right wall $t^* > 0$, $x = L$:	$u = v = 0$,	$\frac{\partial T}{\partial x} = 0$ for $0 \leq y \leq 0.25L$
	$0 \leq y \leq L$:	$T = T_h$ for $0.25L \leq y \leq 0.75L$
		$\frac{\partial T}{\partial x} = 0$ for $0.75L \leq y \leq L$
Bottom wall $t^* > 0$, $y = 0$:	$u = v = 0$,	$\frac{\partial T}{\partial y} = 0$ for $0 \leq x \leq 0.25L$
	$0 \leq x \leq L$:	$T = T_c$ for $0.25L \leq x \leq 0.75L$
		$\frac{\partial T}{\partial y} = 0$ for $0.75L \leq x \leq L$
Top wall $t^* > 0$, $y = L$:	$u = v = 0$	$\frac{\partial T}{\partial y} = 0$ for $0 \leq x \leq 0.25L$
	$0 \leq x \leq L$:	$T = T_c$ for $0.25L \leq x \leq 0.75L$
		$\frac{\partial T}{\partial y} = 0$ for $0.75L \leq x \leq L$

TABLE II. Thermo-physical properties of water, kerosene, Fe_3O_4 and $MWCNT$.[53,54]

Property	Water	Kerosene	Fe_3O_4	MWCNT
$\rho(kgm^{-3})$	$997 \cdot 1$	780	5200	1600
$C_p(Jkg^{-1}K^{-1}$	4179	2090	670	796
$k(Wm^{-1}k^{-1})$	$0 \cdot 613$	$0 \cdot 149$	6	3000
$\beta(K^{-1})$	21×10^{-5}	99×10^{-5}	$1 \cdot 3 \times 10^{-5}$	$4 \cdot 2 \times 10^{-5}$
$\sigma(\Omega^{-1}m^{-1})$	$0 \cdot 05$	6×10^{-10}	25×10^3	$4 \cdot 8 \times 10^{-7}$
$\mu(kgm^{-1}s^{-1})$	$8 \cdot 9 \times 10^{-4}$	$1 \cdot 64 \times 10^{-3}$	-	-

TABLE III. Dimensionless parameters

Reynolds number	$Re = \frac{U_0 L}{\nu_f}$
Grashof number	$Gr = \frac{g\beta_f (T_h - T_c) L^3}{\nu_f^2}$
Prandtl number	$Pr = \frac{\nu_f}{\alpha_f}$
Hartmann number	$Ha = B_0 L \sqrt{\frac{\sigma_f}{\mu_f}}$
Richardson number	$Ri = \frac{Gr}{Re^2}$
Heat generation/absorption coefficient	$Q = \frac{Q_0 L^2}{(\rho C_p)_{hnf} \alpha_{hnf}}$
Darcy number	$Da = \frac{K}{L^2}$
Cattaneo-Christov heat flux parameter	$\delta_e = \frac{\delta U_0}{L}$

III. MAC SOLUTION AND VALIDATION OF MAC RESULTS

The MAC method is used to solve the Eqns. (7)-(9) with non-dimensional initial-boundary conditions as stated in Table 4. The detailed explanation about the MAC procedure is found in the references.[21,49,50,55,56] The discretization form of momentum and energy equations are presented as follows.

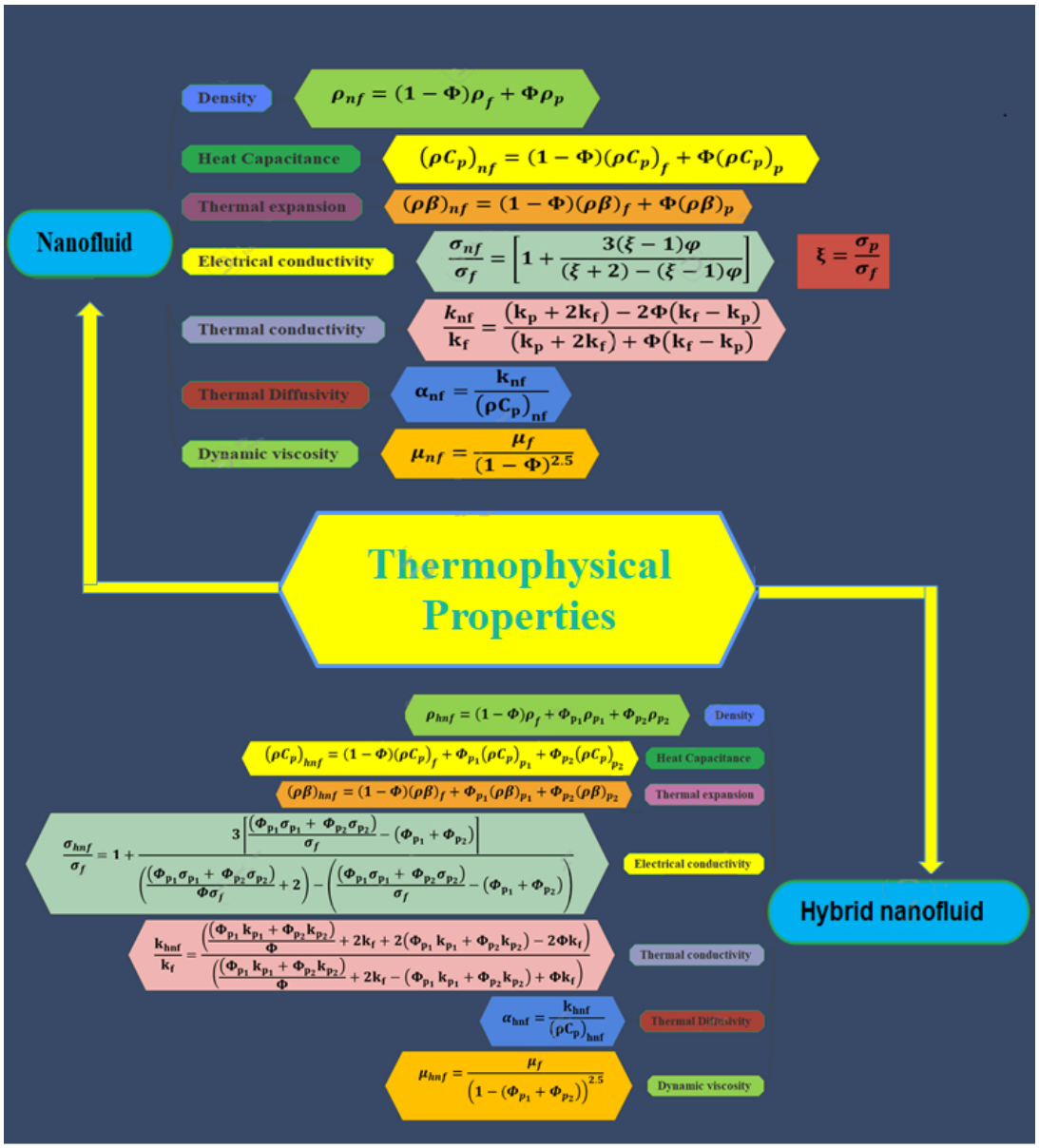

FIG. 2. Thermophysical properties of mono and hybrid nanofluids[52]

The X-momentum equation is discretized as:

$$U^{n+1} = U^n + \left(-\left[U\frac{\partial U}{\partial X} + V\frac{\partial U}{\partial Y}\right] + A_1\left[\frac{\partial^2 U}{\partial X^2} + \frac{\partial^2 U}{\partial Y^2}\right]\right)dt - \left(A_2 U + A_3\, U\sqrt{U^2+V^2}\right)dt. \tag{12}$$

The Y-momentum equation is discretized as:

$$V^{n+1} = V^n + \left(-\left[U\frac{\partial V}{\partial X} + V\frac{\partial V}{\partial Y}\right] + A_1\left[\frac{\partial^2 V}{\partial X^2} + \frac{\partial^2 V}{\partial Y^2}\right]\right)dt - \left(A_2 V - A_4\,\theta + A_3\, V\sqrt{U^2+V^2} + A_5 V\right)dt. \tag{13}$$

The discretized energy equation to obtain the next time level (θ^{n+1}) is acquired as follows:

$$\theta^{n+1} = \theta^n + \left(-\left[U\frac{\partial \theta}{\partial X} + V\frac{\partial \theta}{\partial Y}\right] + A_6\left[\frac{\partial^2 \theta}{\partial X^2} + \frac{\partial^2 \theta}{\partial Y^2} + Q\theta\right]\right)dt - \left[\delta_e\left(U\frac{\partial U}{\partial X}\frac{\partial \theta}{\partial X} + V\frac{\partial V}{\partial Y}\frac{\partial \theta}{\partial Y} + U^2\frac{\partial^2 \theta}{\partial X^2} + V^2\frac{\partial^2 \theta}{\partial Y^2}\right)\right]dt - \left[\delta_e\left(2UV\frac{\partial^2 \theta}{\partial X \partial Y} + U\frac{\partial V}{\partial X}\frac{\partial \theta}{\partial Y} + V\frac{\partial U}{\partial Y}\frac{\partial \theta}{\partial X}\right)\right]dt. \tag{14}$$

where, $A_1 = \left(\frac{\nu_{hnf}}{\nu_f}\right)\frac{1}{Re}$, $A_2 = \left(\frac{\nu_{hnf}}{\nu_f}\right)\frac{1}{ReDa}$ $A_3 = \frac{F}{\sqrt{Da}}$, $A_4 = \frac{(\rho\beta)_{hnf}}{\rho_{hnf}\beta_f}\,Ri$, $A_5 = \left(\frac{\rho_f}{\rho_{hnf}}\right)\left(\frac{\sigma_{hnf}}{\sigma_f}\right)\frac{Ha^2}{Re}$, $A_6 = \left(\frac{\alpha_{hnf}}{\alpha_f}\right)\frac{1}{Re\,Pr}$.

TABLE IV. The dimensionless initial-boundary conditions[21,47]

Initial condition $t \leq 0$, $0 \leq X \leq 1$, $0 \leq Y \leq 1$:	$U = V = 0$	$\theta = 0$
Left wall $t > 0$, $X = 0$:	$U = V = 0$,	$\frac{\partial \theta}{\partial X} = 0$ for $0 \leq Y \leq 0.25$
	$0 \leq Y \leq 1$:	$\theta = 1$ for $0.25 \leq Y \leq 0.75$
		$\frac{\partial \theta}{\partial X} = 0$ for $0.75 \leq Y \leq 1$
Right wall $t > 0$, $X = 1$:	$U = V = 0$,	$\frac{\partial \theta}{\partial X} = 0$ for $0 \leq Y \leq 0.25$
	$0 \leq Y \leq 1$:	$\theta = 1$ for $0.25 \leq Y \leq 0.75$
		$\frac{\partial \theta}{\partial X} = 0$ for $0.75 \leq Y \leq 1$
Bottom wall $t > 0$, $Y = 0$:	$U = V = 0$,	$\frac{\partial \theta}{\partial Y} = 0$ for $0 \leq X \leq 0.25$
	$0 \leq X \leq 1$:	$\theta = 0$ for $0.25 \leq X \leq 0.75$
		$\frac{\partial \theta}{\partial Y} = 0$ for $0.75 \leq X \leq 1$
Top wall $t > 0$, $Y = 1$:	$U = V = 0$	$\frac{\partial \theta}{\partial Y} = 0$ for $0 \leq X \leq 0.25$
	$0 \leq X \leq 1$:	$\theta = 0$ for $0.25 \leq X \leq 0.75$
		$\frac{\partial \theta}{\partial Y} = 0$ for $0.75 \leq X \leq 1$

To demonstrate the accuracy of the MAC numerical scheme, the present outcomes are compared with Khan et al.[50] in a special case. The hybrid nanofluid's thermophysical properties, magnetic field, heat source/sink, and Cattaneo Christov heat flux, are considered to be absent, the thermal radiation is considered to be present, and adequate adjustments are made in the initial and boundary conditions of the current model to compare the current outcomes with the results presented by Khan et al.[50]. One can observe from Figure 3 that the current MAC results which are illustrated through the streamlines and isotherms contours express a substantial agreement with the outcomes of Khan et al.[50]. This validates the accurateness of the current outcomes.

IV. RESULT AND DISCUSSION

In this section, the MAC numerical results (contour plots and graphs) are presented and scrutinized for the magneto-hydrodynamic free convection inside a square porous enclosure filled with the $Fe_3O_4 - MWCNT-$water or $Fe_3O_4 - MWCNT-$kerosene hybrid nanofluid with heat sink/source and Cattaneo–Christov heat flux. The range of key parameters is specified as follows: volumetric heat generation/absorption coefficient $(-5 \leq Q \leq 15)$, nanoparticle volume fraction $(0.01 \leq \phi \leq 0.05)$, Richardson number $(10^{-2} \leq Ri \leq 10)$, Darcy number $(10^{-3} \leq Da \leq 10^{-1})$, Reynolds number $(1 \leq Re \leq 5)$, Hartmann number $(0 \leq Ha \leq 50)$, and Prandtl number $(Water = 6.8 \ \& \ Kerosene = 21.003)$. The following default values are employed throughout the simulations: $Re = 5$, $Q = -5$, $Da = 10^{-3}$; $Ha = 10$, $\phi = 0.05$, $Ri = 1$, and $\delta_e = 0.01$, unless otherwise specified. This data correlates as closely as possible to the actual operational characteristics of hybrid electromagnetic fuel cells by deploying the hybrid nanofluids[54,57,58]. Figures $4-21$ portray the outcomes of these parameters on average heat transfer rate, local heat transfer rate, streamlines, isotherms, U and V velocity profiles. Further, the average Nusselt number distribution is demonstrated in Tables $5-6$.

A. Investigating the streamlines and isotherms profiles under the consequence of Reynolds number

In fluid mechanics, the Reynolds number is a dimensionless quantity that estimates the proportion of inertia force to viscous force. This ratio is influenced by different factors, including the fluid velocity variations. The Reynolds number

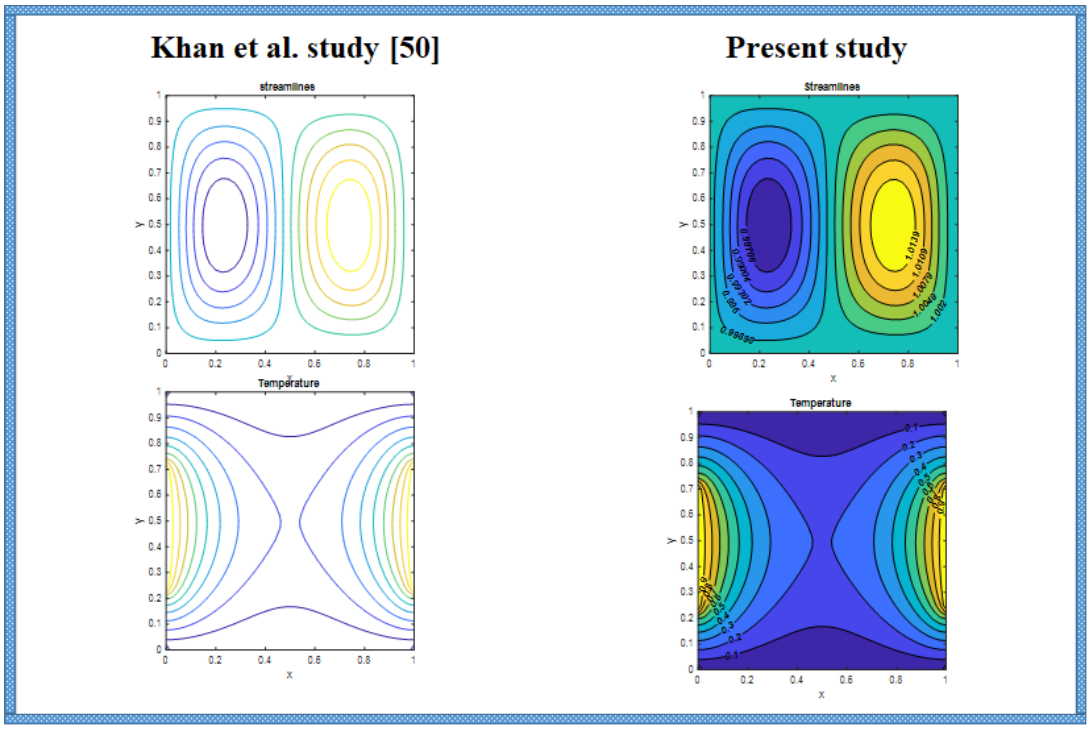

FIG. 3. Comparative contour plots with $Gr = 10^4$, $Re = 10$, $Pr = 0.71$, $Da = 10^{-2}$, $Nr = 1$.[50]

helps to predict the flow patterns in various flow situations. Higher Reynolds numbers represent the turbulent flow while the lower Reynolds numbers represent the laminar flow. The Reynolds number is one of the important pertinent parameters in fluid mechanics. Figure 4 shows the streamline distributions inside the square enclosure with different Reynolds number (Re) for both $Fe_3O_4 - MWCNT-$water (Fig. 4-I) and $Fe_3O_4 - MWCNT-$kerosene (Fig. 4-II) hybrid nanofluids. The values of the inner circulation cells gradually increase and the flow is more elevated at the top and bottom of the cavity when the values of Reynolds number are magnified. In Fig. 4-I, dual circulation cells are formed in case of $Fe_3O_4 - MWCNT-$water hybrid nanofluid when $Re = 1$. For the higher values of Reynolds number, the circulating cells are stretched along the vertical direction, and higher circulations are observed at bottom and top of the enclosure. However, in the center of the cavity, the flow is reduced. In $Fe_3O_4 - MWCNT-$kerosene hybrid nanofluid case, when $Re = 1$, the dual circulation cells are formed inside the enclosure. When the Reynolds number is augmented from $Re = 1$ to $Re = 3$, the circulating cells are fragmented. This implies that velocity of the hybrid nanofluid is reduced at the middle part of the enclosure and the fluid velocity is increased at the bottom and top of the enclosure. For the higher values of Reynolds number, the inner circulating cells are broken into two portions and slightly move towards the top and bottom walls of the cavity. As a result, it is notable that in the case of $Fe_3O_4 - MWCNT-$kerosene hybrid nanofluid, stronger circulation is observed at the top and bottom regions of the cavity and the flow velocity decreases at the center of the cavity.

Figure 5 elucidates the isotherms of $Fe_3O_4 - MWCNT-$water (Fig. 5-I) and $Fe_3O_4 - MWCNT-$kerosene (Fig. 5-II) hybrid nanofluids within the cavity for various values of Reynolds number. As seen in Fig. 5 (I-A), energy transfer inside the cavity is suppressed with a cooler central zone when $Re = 1$. The effect of the cold slits is dominant in the center of the cavity whereas the impact of hot slits is explored only in their neighborhoods. When $Re = 3$, the influence of the hot slits and cold slits is relatively same inside the cavity as shown in Fig. 5 (I-B). When $Re = 5$, the influence of the hot slits is dominant in the center of the cavity whereas the impact of cold slits is explored only in their neighborhoods. The results indicate that the energy transfer is considerably improved for augmenting the Reynolds number. The heat transfer analysis of $Fe_3O_4 - MWCNT-$kerosene hybrid nanofluid is demonstrated in Fig. 5 (II). It is observed that the influence of the hot slits and cold slits is relatively same inside the cavity when $Re = 1$. For increasing the value of Reynolds number from $Re = 1$ to $Re = 3$, the heat transfer is increased in the middle part of cavity as shown in Fig. 5 (II-B). Increasing the values of Reynolds number from $Re = 3$ to $Re = 5$ has the tendency to significantly explore the impact of the hot slits throughout the cavity except the neighborhood of cold slits. This indicates that the heat transfer improves for enhancing the Reynolds number values. The influence of the hot slits is more prominent with more elevated values of Reynolds number.

B. Investigating the effect of the magnetic field of hybrid nanofluids on streamlines, isotherms, U and V velocity profiles

When the applied magnetic field interacts with the electrically conducting fluid, a magnetic force known as the Lorentz force is formed, which affects fluid velocity. In the theoretical analysis of such flows, a dimensionless variable known as the Hartmann number arises which represents the ratio of the magnetic force to viscous force. Figure 6 represents the significance of the Hartmann number values on streamline contours for $Fe_3O_4 - MWCNT-$water (Fig. 6-I) and $Fe_3O_4 - MWCNT-$kerosene (Fig. 6-II) hybrid nanofluids. The magnetic field effect is featured in the Y-momentum $(Eqn.(8))$ through the term $\frac{\rho_f}{\rho_{hnf}}\frac{\sigma_{hnf}}{\sigma_f}\frac{Ha^2}{Re}$. An increase in the values of the Hartmann number boosts the magnetic body force and strongly modifies the inner circulating cells' strength and contour substantially for both hybrid nanofluids. When $Ha = 0$ (in the absence of the magnetic field), the flow circulates freely inside the square cavity. In this case, a single left and right circulation cells are formed for $Fe_3O_4 - MWCNT-$water hybrid nanofluid. The inner circulation cell forms a peanut shell shaped structure. When $Ha =$ 10, there is no change in the shape of the circulating cells but the magnitudes of the stronger circulation cells slightly diminish. When $Ha = 50$, the inner circulating cells are divided into two parts and the magnitudes of the circulating cells are diminished. This elucidates that an augmentation in the Hartmann number causes a deceleration in the fluid flow. As seen in Fig. 6 (II-A), double right and left circulation cells form for $Fe_3O_4 - MWCNT-$kerosene hybrid nanofluid when $Ha = 0$. There is no significant change in the streamlines of $Fe_3O_4 - MWCNT-$kerosene hybrid nanofluid for magnifying the Hartmann number from $Ha = 0$ to $Ha = 10$. Rising the Hartmann number to $Ha = 50$ makes notable change in the eddies. The two eddies emerge at the bottom and top of the cavity walls as shown in Fig. 6(II-C). For the increased values of the Hartmann number, the stronger circulation cell's shapes are slightly changed and more inner circulation cells form at the top and bottom of the cavity. The center of the cavity has less flow; the left circulation cells are entirely broken into two separate circulation cells and the inner layers of the right circulating cells are separated. This means that the fluid velocity is reduced in the middle of the enclosure while it is increased at the bottom and top. That is, the magnetic force suppresses and weakens the circulating cells as the Hartmann number increases. It is noticed from Figs. (6-I) and (6-II) that the impact of magnetic field on $Fe_3O_4 - MWCNT-$kerosene hybrid nanofluid is stronger than $Fe_3O_4 - MWCNT-$water hybrid nanofluid. There is clearly an interplay between the magnetic and viscous forces which produce different effects in the $Fe_3O_4 - MWCNT-$water and $Fe_3O_4 - MWCNT-$kerosene hybrid nanofluids, and this is attributable to viscosity differences in the base fluids.

Figure 7 represents the significance of the Hartmann number on isotherm contours for $Fe_3O_4 - MWCNT-$water and $Fe_3O_4 - MWCNT-$kerosene hybrid nanofluids. For both hybrid nanofluids considerable heat transfer is observed at the center of the cavity. The higher heat transmission is observed near the right and left hot slits in case of $Fe_3O_4 - MWCNT-$ water. Higher heat transfer is observed throughout the cavity except the neighborhoods of the cold slits in $Fe_3O_4 - MWCNT-$kerosene hybrid nanofluid case. Although some kinetic energy is dissipated as thermal energy by dragging the nanofluid against the action of the transverse magnetic field, there is no significant heat transfer modification in both hybrid nanofluids for increasing values of the magnetic parameter. On comparing Figs. 7(I) and 7(II), the heat transfer is greater in the $Fe_3O_4 - MWCNT-$kerosene hybrid nanofluid case. In addition, the impact of hot slits is stronger in $Fe_3O_4 - MWCNT-$kerosene hybrid nanofluid compared to $Fe_3O_4 - MWCNT-$water hybrid nanofluid.

Figure 8 shows the U velocity profiles of $Fe_3O_4 - MWCNT-$water (Fig. 8-I) and $Fe_3O_4 - MWCNT-$kerosene (Fig. 8-II) hybrid nanofluids for different values of the Hartmann number. By increasing the Hartmann parameter from 0 to 10, insignificant changes are obtained in both hybrid nanofluid cases. In the $Fe_3O_4 - MWCNT-$water hybrid nanofluid case, when $Ha = 0$ and $Ha = 10$, the contour lines are densely formed near the horizontal walls and a single circulation cell is formed near the center of the vertical walls. By enhancing the values from 10 to 50, considerable changes are observed. In this case, the contour lines are shrunk near the horizontal walls whereas more circulation cells are formed at the center of the cavity. In the $Fe_3O_4 - MWCNT-$kerosene hybrid nanofluid case, the contour lines are densely formed near the horizontal walls of the cavity for all the considered values of Ha. At the center portion, when $Ha = 0$ and $Ha =$ 10, more circulation cells are formed along the secondary diagonal zone whereas more circulation cells are formed along the principal diagonal zone in the case of $Ha = 50$. Overall, an increase in Ha slightly enhances the circulation at the center.

Figure 9 illustrates the V velocity profiles of $Fe3O4 - MWCNT-$Water (Fig. 9-I) and $Fe3O4 - MWCNT-$kerosene (Fig. 9-II) hybrid nanofluids for various values of the magnetic parameter. As seen in Fig. 9(I-A), combined circulation cells are formed at the middle portion when $Ha = 0$. When $Ha = 10$, the inner contour line shrinks at the middle portion. When $Ha = 50$, the inner cells are split and moved towards the top and bottom zones. This indicates that improving the magnetic parameter reduces the velocity at the center and increases near the horizontal walls. It is noticed from Fig. 9(II-A) that stronger circulation cells are formed close to the vertical walls when $Ha = 0$. When $Ha = 10$, the stronger circulation cells slightly shrink at the middle portion but the weaker circulation cells are densely formed at the center of the cavity. When high magnetic field $(Ha = 50)$ is imposed, the stronger circulation cells near the vertical wall are split into two parts and slightly move towards the horizontal walls and the dense of the inner contour lines is decreased, as seen in Fig. 9(II-C). Therefore, an increase in the values of the magnetic parameter reduces the V-velocity profiles in the center of the cavity.

C. Investigating the consequence of Darcy on streamlines and isotherms

The Darcy number (Da) quantifies the effect of porous medium's permeability (K) on the percolating nanofluid. A reduction in K means an increase in flow resistance. This porous solid matrix's fiber structure significantly affects the fluid flow characteristics and considerably affects the heat transfer characteristics. The Darcy parameter arises in both primary and secondary momentum equations ($Eqns.(7)$ and (8)) through the linear Darcy drag force terms, $\frac{-\nu_{hnf}}{\nu_f}\frac{1}{ReDa}U$ and $\frac{-\nu_{hnf}}{\nu_f}\frac{1}{ReDa}V$. In this study, permeability of the porous matrix is considered based on the physically attainable range ($10^{-3} \leq Da \leq 10^{-1}$). Figure 10 displays the Darcy parameter's influence on streamlines distribution of $Fe_3O_4 - MWCNT-$water and $Fe_3O_4 - MWCNT-$kerosene hybrid nanofluids. As seen, the circulating cells in the $Fe_3O_4 - MWCNT-$water hybrid nanofluid case are created along the center portion of the cavity whereas the circulating cells in the $Fe_3O_4 - MWCNT-$kerosene hybrid nanofluid case are divided into two eddies and are formed at the bottom and top of the enclosure. Enhancing values of the Darcy number modify the inner circulation cells gradually and the flow is increased at the center of the cavity in the $Fe_3O_4 - MWCNT-$water hybrid nanofluid case. The inner circulating cells are enlarged and extended towards the center of the enclosure in $Fe_3O_4 - MWCNT-$kerosene hybrid nanofluid case. This shows that increasing values of Darcy parameter increase the fluid flow inside the enclosure.

Figure 11 demonstrates the influences of the Darcy number on isotherm contours for $Fe_3O_4 - MWCNT-$water and $Fe_3O_4 - MWCNT-$kerosene hybrid nanofluids. In the contour plots, for both hybrid nanofluids, significant heat transfer is observed at center of the cavity i.e. thermal diffusion is intensified in the central zone of the cavity. In case of $Fe_3O_4 - MWCNT-$water hybrid nanofluid, higher temperature contour's magnitude is observed near the right and left hot slits as shown in Fig. 11(I). In $Fe_3O_4 - MWCNT-$kerosene hybrid nanofluid case stronger heat transfer is observed throughout the cavity and more variations in the heat transfer are noticed near the cold slits. Comparing Figs. 11(I) and 11(II), more efficient thermal transport arises in the $Fe_3O_4 - MWCNT-$kerosene hybrid nanofluid case in which a warmer (yellow) central zone is consistently visible whereas in the $Fe_3O_4 - MWCNT-$water hybrid nanofluid case, slightly cooler (dark orange) central zones are observed.

D. Investigating the consequence of heat absorption and generation on streamlines, isotherms, U and V velocity profiles

A heat sink is a passive heat exchanger that transmits the heat produced by a mechanical or electronic devices into a coolant fluid in motion. A heat source is an object that produces or radiates heat. It should be emphasized that $Q < 0$ signifies the internal heat sink (absorption) whereas $Q > 0$ characterizes the internal heat source (generation). Figure 12 illustrates the impacts of heat absorption/generation (Q) on the streamlines for $Fe_3O_4 - MWCNT-$water (Fig. 12-I) and $Fe_3O_4 - MWCNT-$kerosene (Fig. 12-II) hybrid nanofluids. In the $Fe_3O_4 - MWCNT-$water hybrid nanofluid case with heat sink ($Q = -5$) impact, there are two parallel elongated vertical cells which are distributed in the enclosure. For the $Fe_3O_4 - MWCNT-$kerosene hybrid nanofluid case, there are four cells on which two cells are formed in the right and other two cells are formed in the left half spaces of the cavity when a heat sink is present ($Q = -5$). In the scarcity of heat absorption/generation ($Q = 0$) parameter, in the $Fe_3O_4 - MWCNT-$water case, the inner circulation cells are split and moved towards the bottom and top of the enclosure. The circulation cells shrink at the center of the cavity in $Fe_3O_4 - MWCNT-$kerosene hybrid nanofluid case. The fluid flow is restricted in the cavity compared to the sink case for both hybrid nanofluids. In the heat generation case, ($Q = 15$) case, the cell structure is further modified. For the $Fe_3O_4 - MWCNT-$water hybrid case, two further cells form and now six circulation cells are observed. The circulation cells with low intensity form at the top-left, middle-right and lower-left corner of the enclosure while stronger circulation cells form at the top-right, middle-left and lower-right corner of the enclosure. For the $Fe_3O_4 - MWCNT-$kerosene hybrid nanofluid case, although six cells are present, the central cells are much weaker and not fully formed. The upper and lower pairs of circulation cells are however quite strong with intense flow in the top-right and lower-right corners of the enclosure.

Figure 13 illustrates the influence of heat absorption/generation (Q) on the isotherms for $Fe_3O_4 - MWCNT-$water and $Fe_3O_4 - MWCNT-$kerosene hybrid nanofluids. The modifications in the heat absorption/generation characteristics have a notable impact on heat transfer characteristics inside the cavity. The features of heat absorption/generation parameters on the isotherms of $Fe_3O_4 - MWCNT-$water hybrid nanofluid is shown in Fig. 13-I. As shown, the influence of the hot slits is low at the center zone of the cavity in the case of heat sink ($Q = -5$). In the absent of the internal heat absorption/generation ($Q = 0$), the influence of the hot slits is extended towards the cavity's center region. When the heat source ($Q = 15$) is present, the influence of the hot slits is highly noticeable in the center zone and more heat transfer occurs in the middle of the cavity. Figure (13-II) shows that larger hot zone region arises in the $Fe_3O_4 - MWCNT-$kerosene hybrid nanofluid case. The hot region is sustained in the majority of the cavity and indicating an elevation in heat transfer throughout the cavity. Compared to the heat sink case, the hot region is more extended in the absence of heat sink/source. The deployment of a heat source significantly improves the magnitudes of the isotherms and thereby the energy transfer inside the cavity is enhanced. The influence of heat sink/source is considerably greater in the $Fe_3O_4 - MWCNT-$kerosene hybrid nanofluid compared to $Fe_3O_4 - MWCNT-$water hybrid nanofluid. However, the impact of heat sink/source elucidates higher variations in case of $Fe_3O_4 - MWCNT-$water hybrid nanofluid. As seen in figures (13-I) and (13-II), the variations in the heat sink and source parameter effectively modify the heat transfer in both

hybrid nanofluids.

Figure 14 shows the U velocity profiles of $Fe_3O_4 - MWCNT-$water (Fig. 14-I) and $Fe_3O_4 - MWCNT-$kerosene (Fig. 14-II) hybrid nanofluids for different values of heat source/sink coefficient (Q). When $Q = -5$, the contour lines are densely formed near the horizontal walls and a single circulation cell is formed near the center of the vertical walls. When $Q = 0$, the contour lines are shrunk near the top horizontal walls whereas few circulation cells are formed at the center of the cavity. When $Q = 15$, the contour lines are further shrunk near the horizontal walls whereas more circulation cells are formed at the center of the cavity. In the $Fe_3O_4 - MWCNT-$kerosene hybrid nanofluid case, the contour lines are densely formed near the horizontal walls of the cavity for all the considered values of Q. When increasing the values of Q, more circulation cells are formed at the middle of cavity. Overall, an increase in Q slightly enhances the circulation at the center.

Figure 15 illustrates the V velocity profiles of $Fe_3O_4 - MWCNT-$water (Fig. 15-I) and $Fe_3O_4 - MWCNT-$kerosene (Fig. 15-II) hybrid nanofluids for various values of heat source/sink coefficient (Q). As seen in Fig. 15(I-A), combined circulation cells are formed at the middle portion when $(Q = -5)$. When $(Q = 0)$, the inner cells are split and moved towards the top and bottom zones. When $(Q = 15)$, stronger circulation cells are noticed inside the cavity but weaker circulation cells are noticed near the center of the vertical and horizontal walls. As seen, fluid circulation is very high in the presence of heat source. It is noticed from Fig. 15(II-A) that stronger circulation cells are formed close to the vertical walls when $(Q = -5)$. When $(Q = 15)$, the stronger circulation cells near the vertical wall are split into two parts and slightly move towards the horizontal walls and the dense of the inner contour lines is decreased, as seen in Fig. 15(II-C). Overall, an enhancement in the values of the heat source/sink coefficient Q increases the V-velocity profiles in the center of the cavity.

E. Investigating the streamline profiles under the consequence of Richardson number

Figure 16 portrays the forced convective (A), mixed convective (B), and natural convective (C) fluid flow characteristics of both $Fe_3O_4 - MWCNT-$water (Fig. 16-I) and $Fe_3O_4 - MWCNT-$kerosene (Fig. 16-II) hybrid nanofluids. The convective transportation within the cavity is greatly influenced by the Richardson number. The Richardson number represents the connection between the buoyancy effects and shear force and is expressed as $Ri = \frac{Gr}{Re^2}$. Higher Richardson numbers indicate the natural convective flow $(Ri > 1)$, lower Richardson numbers indicate the forced convective flow $(Ri < 0.1)$, and $Ri = 1$ describes the pure mixed convective flow. The thermal buoyancy term $\frac{\rho\beta_{hnf}}{\rho_{hnf}\beta_f} Ri\theta$ contains the Richardson number and it is considered in the secondary momentum equation $(Eqn.8)$. Figure 16 (I-A) visualizes the development of streamlines for $Fe_3O_4 - MWCNT-$water and $Fe_3O_4 - MWCNT-$kerosene hybrid nanofluids flow in the case of natural convection i.e. $Ri = 10$. In the $Fe_3O_4 - MWCNT-$water hybrid nanofluid case, more circulating cells are formed in the proximity of the right wall with strong flow movement in the middle core region of the enclosure. On the other hand, in the $Fe_3O_4 - MWCNT-$kerosene hybrid nanofluid case, the circulating cells have separated into two different eddies and are created along the cavity's top and bottom walls. As a result, in the middle of the cavity, there is less flow. The contour shapes are not noticeably modified when Ri is improved from 0.01 to 1 (i.e. forced convective flow to mixed convective flow) for both hybrid nanofluids. This reveals that even in the case of mixed convection, the forced convective flow behavior is maintained consistently. When $Ri = 10$, the magnitudes of the interior vortices are increased for both nanofluids as shown in Figure 16(C). The magnitude of streamline contours is more elevated in $Fe_3O_4 - MWCNT-$water hybrid nanofluid compared to $Fe_3O_4 - MWCNT-$kerosene hybrid nanofluid. Further, a dual eddy pair is noticed inside the enclosure for the $Fe_3O_4 - MWCNT-$water hybrid nanofluid whereas a quadruple eddy structure is observed with the $Fe_3O_4 - MWCNT-$kerosene hybrid nanofluid for any value of Richardson number. This indicates that higher velocity is observed in $Fe_3O_4 - MWCNT-$water hybrid nanofluid compared to $Fe_3O_4 - MWCNT-$kerosene hybrid nanofluid.

F. Investigating the effect of the volume fraction of hybrid nanoparticles on streamlines and isotherms

The fluid's ability to transfer the heat is mainly governed by its thermal conductivity. The addition of nanoparticles has the tendency to enhance the thermal conductivity of the carrying fluid. In addition, the proper combination of different variety of nanoparticles further augments the thermal conductivity of the carrying fluid. As a result, the behavior of streamlines of the hybrid nanofluids is modified for increasing the volume fraction of the hybrid nanoparticles. It is to be noted that the impact of volume fraction is analyzed by fixing the heat sink/source parameter value as $Q = 15$ (heat source). Figure 17 demonstrates the streamlines of $Fe_3O_4 - MWCNT-$water (Figure 17-I) and $Fe_3O_4 - MWCNT-$kerosene (Figure 17-II) hybrid nanofluids. In the $Fe_3O_4 - MWCNT-$water hybrid nanofluid case, circulation cells form throughout the cavity, with stronger flow synthesizes along the corners of right-side wall and the center of left-side wall. In the $Fe_3O_4 - MWCNT-$kerosene hybrid nanofluid case, the circulating cells form in the corners of the enclosure, the stronger flow synthesizes along the corners of right-side wall, and the minimum number of circulation cells is formed in the center of the right and left walls. This implies that an insignificant flow is noticed in the core zone of the cavity in the case of $Fe_3O_4 - MWCNT-$kerosene hybrid nanofluid. Figure (17-I) shows that for increasing the values of ϕ, the shape of the stronger circulation cells enlarges whereas the weaker circulation cells shrink. These changes are more noticeable for increasing the volume fraction from $\phi = 0.03$ to $\phi = 0.05$. Therefore, the flow circulation inside

the cavity is increasing for increasing the volume fraction. Figure (17-II) explores that for increasing the values of volume fraction (ϕ), the magnitudes of the weaker circulation cells are slightly increased whereas there is no variation in the magnitudes of the stronger circulation cells. In addition, there is no change in the shape of the circulation cells. This indicates that the volume fraction variation has a slight impact on the flow characteristics of $Fe_3O_4 - MWCNT-$kerosene hybrid nanofluid. The variation in the volume fraction is more effective in $Fe_3O_4 - MWCNT-$water hybrid nanofluid compared to $Fe_3O_4 - MWCNT-$kerosene hybrid nanofluid.

Figure 18 indicates the impact of the volume fraction factor (ϕ) on isotherms for $Fe_3O_4 - MWCNT-$water (Fig. 18-I) and $Fe_3O_4 - MWCNT-$kerosene (Fig. 18-II) hybrid nanofluids. Figures 18 (I-A), 18 (I-B), and 18 (I-C) and 18 (II-A) in order, explain the attributes of isotherms of $Fe_3O_4 - MWCNT-$water hybrid nanofluid with $1\%, 3\%$, and 5% nanoparticles volume fraction. In case of $Fe_3O_4 - MWCNT-$water hybrid nanofluid, higher heat transmission is noticed in the center of the cavity. More circulating cells are originated at the bottom and top of the cavity whereas few circulation cells are formed near the hot slits and the center of the cavity. There is no significant variation in the shape of the isotherms for increasing the nanoparticle's volume fraction. However, the magnitudes are considerably increased for increasing the nanoparticle's volume fraction. In addition, it is well known that the heat transfer rate is dependent on the concentration (percentage doping) of nanoparticle's volume fraction. As a result, the heat transmission characteristics of the hybrid nanofluids are enhanced extensively with a boost in the nanoparticle volume fraction. Figures 18 (II-A), 18 (II-B) and 18 (II-C) in order elucidate the features of $Fe_3O_4 - MWCNT-$kerosene hybrid nanofluid with $1\%, 3\%$, and 5% nanoparticles volume fraction. Increasing the mixture of volume fraction clearly induces modifications in the magnitudes of the isotherms inside the cavity but there is no change in the shape of the isotherms. In $Fe_3O_4 - MWCNT-$kerosene hybrid nanofluid case, the impact of internal heat generation is very high in the center of the cavity as well as it is expanded in all the directions within the cavity. Most of the heat transfer variations are noticed at the bottom and top sides of the enclosure where the cold slits are considered whereas a single heat transfer variation is observed on the right and left wall sides where the hot slits are considered. It is noticed that greater heat transfer is observed in the $Fe_3O_4 - MWCNT-$kerosene hybrid nanofluid case compared to $Fe_3O_4 - MWCNT-$water hybrid nanofluid.

G. Characteristics of Nusselt number distribution

Figure 19 illustrates the local heat transfer rate for various volume fraction values. For enhancing the hybrid nanoparticle's volume fractions, the local Nusselt number profiles are increased. i.e. greater percentage of doping the nanoparticles boosts the heat transferred at the boundaries of the enclosure. More noticeable modifications are observed in the $Fe_3O_4 - MWCNT-$kerosene hybrid nanoliquid case compared to the $Fe_3O_4 - MWCNT-$water hybrid nanoliquid case. The attributes of the average heat transfer rate for different values of volume fraction are demonstrated in Table 5. Apparently, there is a significant variation in the mean heat transfer rate of water and kerosene based nanofluids. The average heat transfer rates of $Fe_3O_4 - MWCNT-$water and $Fe_3O_4 - MWCNT-$kerosene hybrid nanofluids differ by 10.93% when 1% of hybrid nanoparticles are suspended into the base-fluids. The mean heat transfer rate of $Fe_3O_4 - MWCNT-$kerosene hybrid nanofluid is more elevated than $Fe_3O_4 - MWCNT-$water hybrid nanofluid. When 3% of $Fe_3O_4 - MWCNT$ hybrid nanoparticles are suspended into water and kerosene base fluids, the mean heat transfer rate of $Fe_3O_4 - MWCNT-$kerosene hybrid nanofluid is 8.88% higher than that of $Fe_3O_4 - MWCNT-$water hybrid nanofluid. When 5% of $Fe_3O_4 - MWCNT$ nanoparticles are suspended into water and kerosene, the difference in the mean heat transfer rate between $Fe_3O_4 - MWCNT-$water and $Fe_3O_4 - MWCNT-$kerosene hybrid nanofluids is 6.81%.

The impact of the heat sink or source parameters on the local rate of heat transfer is depicted in Fig. 20. Increased heat source parameter values $(Q = +15)$ enrich the local Nusselt number profiles, whereas increasing heat sink parameter values $(Q = -5)$ suppresses the local Nusselt number profiles. $Q = 0$ denotes the non-existence of heat source/sink. In addition, more elevated heat transfer rates are computed in the case of $Fe_3O_4 - MWCNT-$water hybrid nanofluid. Table 6 depicts the mean heat transfer rate characteristics for various heat sink and source parameter values. In the presence of a heat sink, the average heat transfer rate of $Fe_3O_4 - MWCNT-$water hybrid nanofluid is 78.92% lower than that of $Fe_3O_4 - MWCNT-$kerosene hybrid nanofluid. In the absence of a heat sink/source, the average heat transfer rate of $Fe_3O_4 - MWCNT-$kerosene hybrid nanofluid is 57.62% higher than that of $Fe_3O_4 - MWCNT-$water hybrid nanoliquid. In the presence of a heat source, the average heat transfer rate of $Fe_3O_4 - MWCNT-$kerosene hybrid nanofluid is 6.81% higher than that of $Fe_3O_4 - MWCNT-$water nanofluid. As a result, the increment in the mean heat transfer rate for the investigated nanoliquids varies greatly with changes in heat absorption/generation within the porous cavity. In addition, more elevated heat transfer occurs in the case of $Fe_3O_4 - MWCNT-$kerosene hybrid nanofluid.

Figure 21 examines the influence of non-Fourier thermal relaxation parameter δ on non-dimensional temperature of both $Fe_3O_4 - MWCNT-$water and $Fe_3O_4 - MWCNT-$kerosene hybrid nanofluids. The Nusselt number is seen to have an inverse relationship with the thermal relaxation parameter. The trends substantiate the Cattaneo-Christov theory that the higher values of (δ_e) physically imply that greater time is needed to transfer heat to particles with low energy when a temperature gradient is present in the medium. The thermal relaxation effect therefore delays heat transmission in nanofluids. It is to be noted that for $(\delta_e = 0)$, the classical Fourier conduction case is retrieved, and in this case, energy transfers without any time lag through the entire medium of the cav-

TABLE V. Variations of hybrid nanofluids' average heat transfer rate with various volume fraction values

Parameter Values	$Fe_3O_4-MWCNT-$water	$Fe_3O_4-MWCNT-$kerosene
$\Phi=0.01$	4.168388139867347	4.624275837501220
$\Phi=0.03$	4.454226967509394	4.850175712758110
$\Phi=0.05$	4.760691225892772	5.085262819964906

TABLE VI. Variations of average heat transfer rate with various heat source/sink parameter values

Parameter Values	$Fe_3O_4-MWCNT-$water	$Fe_3O_4-MWCNT-$kerosene
$Q=-5$	2.305576754043674	4.125313772987758
$Q=0$	2.757630803341192	4.346837999491187
$Q=15$	4.760691225892772	5.085262819964906

ity. From Fig. 21, it is evident that the temperature is higher for the case of Fourier's model ($\delta_e=0$) than that of the Cattaneo–Christov heat flux model ($\delta_e\neq 0$). The inclusion of the non-Fourier hyperbolic heat conduction model therefore avoids the over-prediction of temperatures associated with the classical Fourier parabolic heat conduction model. In addition, the Cattaneo–Christov heat flux model can represent a material's conducting or non-conducting nature. Further, there is a notable variation in the heat transfer rate estimated with different base fluids (water & kerosene).

V. CONCLUSIONS

The magnetohydrodynamic mixed convective hybrid nanofluid flow inside a square cavity saturated with a porous medium is studied theoretically. The present investigation addresses the relative heat transfer performance of $Fe_3O_4-MWCNT-$water and $Fe_3O_4-MWCNT-$kerosene hybrid nanofluids within the cavity. The major conclusions of the present numerical problem are mentioned below:

1. An increase in the Hartmann number diminishes the fluid flow intensity in the middle of the cavity and increases at the top and bottom zones.

2. In the case of the $Fe_3O_4-MWCNT-$water hybrid nanofluid, increasing values of the Darcy parameter increase the flow at the cavity's center. The magnitudes of the interior circulating cells in the $Fe_3O_4-MWCNT-$kerosene hybrid nanofluid case are augmented at the top and bottom of the cavity.

3. Increasing values of Reynolds number increase the energy transmission throughout the cavity in $Fe_3O_4-MWCNT-$kerosene case. Further noticed that $Fe_3O_4-MWCNT-$kerosene hybrid nanofluid has a higher energy transfer efficiency than $Fe_3O_4-MWCNT-$water hybrid nanofluid.

4. In forced convection mode, the fluid velocity is greater in the entire cavity for the $Fe_3O_4-MWCNT-$water hybrid nanofluid compared to $Fe_3O_4-MWCNT-$kerosene hybrid nanofluid.

5. When 5% nanoparticles are suspended into water and kerosene base-fluids, the average heat transfer of $Fe_3O_4-MWCNT-$kerosene hybrid nanofluid is 6.81% higher than $Fe_3O_4-MWCNT-$water hybrid nanofluid.

6. Compared to the $Fe_3O_4-MWCNT-$kerosene hybrid nanofluid, the average heat transfer rate of the $Fe_3O_4-MWCNT-$water hybrid nanofluid is 78.92% lower in the presence of the heat absorption effect.

7. Fourier's model achieves higher temperatures than the Cattaneo–Christov heat flux model.

The current investigation has revealed some luring aspects of mixed, forced, and natural convective electro-magneto-hybrid nanofluid flow and energy transmission within a square porous cavity. $Fe_3O_4-MWCNT$ hybrid nanoparticles are suspended into two types of conventional fluids. The MAC algorithm (finite difference) is very advanced and uncomplicated for computing the fluid flow problems which may have some relevance to electro conductive hybrid magnetic nano-fuel cells.

VI. ACKNOWLEDGEMENTS

The second author (Sivaraj Ramachandran) is thankful to the Ministry of Education, United Arab Emirates for the financial assistance to complete this research work through the Collaborative Research Program Grant 2019 (CRPG 2019) with the fund number 21S107.

VII. CONFLICT OF INTEREST

The authors have no conflicts to disclose.

VIII. REFERENCES

[1] A.-Y. Wang, H. Xu, Highly accurate wavelet-homotopy solutions for mixed convection hybrid nanofluid flow in an inclined square lid-driven cavity, Computers & Mathematics with Applications 108 (2022) 88–108.

NOMENCLATURE

x, y	Cartesian coordinates $[m]$
X, Y	Non-dimensional distance along x and y co-ordinates
U_0	Reference velocity $\left[ms^{-1}\right]$
t^*	Dimensional time $[s]$
T	Temperature of fluid $[K]$
L	Length of the enclosure $[m]$
u, v	Velocity components in x, y directions $\left[ms^{-1}\right]$
p	Pressure $[Pa]$
Q_0	Dimensional heat source or sink $[W\ m^{-3}]$
C_p	Specific heat of fluid $[J\ kg^{-1}K^{-1}]$
k	Fluid thermal conductivity $\left[W\ m^{-1}\ K^{-1}\right]$
g	Acceleration due to gravity $\left[m\ s^{-2}\right]$
K	Permeability of the porous medium $\left[m^2\right]$
B_0	Strength of the magnetic field $[kg\ s^{-2}\ A^{-1}]$
U	Non-dimensional velocity component along X direction
V	Non-dimensional velocity component along Y direction
P	Dimensionless pressure
t	Dimensionless time
Ha	Hartmann number
Ri	Richardson number
Gr	Grashof number
Da	Darcy number
Pr	Prandtl number
Q	Heat generation/absorption coefficient
Re	Reynolds number
Nu	Nusselt number
F	Forchheimer coefficient

Greek symbols

θ	Non-dimensional temperature
Φ	Solid volume fraction
β	Thermal expansion coefficient $[K^{-1}]$
σ	Electrical conductivity $[\Omega^{-1}m^{-1}]$
ν	Kinematic viscosity $\left[m^2/s\right]$
ρ	Density of fluid $\left[kg/m^3\right]$
μ	Dynamic viscosity $[kg\ m^{-1}\ s^{-1}]$
α	Thermal diffusivity $[m^2s^{-1}]$
δ	Cattaneo-Christov heat flux parameter
δ_e	Dimensionless Cattaneo-Christov heat flux parameter

Subscripts

h	hot surface
c	cold surface
nf	nanofluid
f	fluid
p_1	Fe_3O_4-nanoparticles
p_2	$MWCNT-$nanoparticles
avg	average
hnf	hybrid nanofluid

[2] A. Yasin, N. Ullah, S. Nadeem, H. A. Ghazwani, Numerical simulation for mixed convection in a parallelogram enclosure: Magnetohydrodynamic (mhd) and moving wall-undulation effects, International Communications in Heat and Mass Transfer 135 (2022) 106066.

[3] K. Mehmood, S. Hussain, M. Sagheer, Numerical simulation of mhd mixed convection in alumina–water nanofluid filled square porous cavity using kkl model: Effects of non-linear thermal radiation and inclined magnetic field, Journal of Molecular Liquids 238 (2017) 485–498.

[4] T. Armaghani, A. Kasaeipoor, N. Alavi, M. Rashidi, Numerical investigation of water-alumina nanofluid natural convection heat transfer and entropy generation in a baffled l-shaped cavity, Journal of Molecular Liquids 223 (2016) 243–251.

[5] S. Baghsaz, S. Rezanejad, M. Moghimi, Numerical investigation of transient natural convection and entropy generation analysis in a porous cavity filled with nanofluid considering nanoparticles sedimentation, Journal of Molecular Liquids 279 (2019) 327–341.

[6] M. A. Sheremet, I. Pop, Effect of local heater size and position on natural convection in a tilted nanofluid porous cavity using ltne and buongiorno's models, Journal of Molecular Liquids 266 (2018) 19–28.

[7] H. Laidoudi, O. D. Makinde, Computational study of thermal buoyancy from two confined cylinders within a square enclosure wifth single inlet and outlet ports, Heat Transfer 50 (2) (2021) 1335–1350.

[8] Z. Khan, O. Makinde, M. Hamid, R. U. Haq, W. Khan, Hydromagnetic flow of ferrofluid in an enclosed partially heated trapezoidal cavity filled with a porous medium, Journal of Magnetism and Magnetic Materials 499 (2020) 166241.

[9] M. Sankar, S. Kiran, G. Ramesh, O. Makinde, Natural convection in a non-uniformly heated vertical annular cavity, Defect and Diffusion Forum 377 (2017) 189–199.

[10] E. G. Ushachew, M. K. Sharma, O. D. Makinde, Numerical study of mhd heat convection of nanofluid in an open enclosure with internal heated objects and sinusoidal heated bottom, Computational Thermal Sciences: An International Journal 13 (5) (2021) 1–16.

[11] A. Hussien, W. Al-Kouz, M. e. a. Hassan, A review of flow and heat transfer in cavities and their applications, Eur. Phys. J. Plus 136 (2021).

[12] D. D. Dixit, A. Pattamatta, Natural convection heat transfer in a cavity filled with electrically conducting nano-particle suspension in the presence of magnetic field, Physics of Fluids 31 (2019) 023302.

[13] A.Bendaraa, M. M. Charafi, A. Hasnaoui, Numerical study of natural convection in a differentially heated square cavity filled with nanofluid in the presence of fins attached to walls in different locations, Physics of Fluids 31 (2019) 052003.

[14] M.Hamid, Z. H. Khan, W. A. Khan, R. U. Haq, Natural convection of water-based carbon nanotubes in a partially heated rectangular fin-shaped cavity with an inner cylindrical obstacle, Physics of Fluids 31 (2019) 103607.

[15] K. S. Arjun, K. Rakesh, Heat transfer in magnetohydrodynamic nanofluid flow past a circular cylinder, Physics of Fluids 32 (2020) 045112.

[16] C.-C. Cho, Natural convection of cu-water nanofluid in enclosed cavity with porous effect and wavy surface based on energy-flux-vector visualization method, Physics of Fluids 32 (2020) 103607.

[17] H. Basha, R. Sivaraj, Exploring the heat transfer and entropy generation of ag/fe3o4-blood nanofluid flow in a porous tube: a collocation solution, Eur. Phys. J. E 44 (2021).

[18] H. Thameem Basha, R. Sivaraj, A. e. a. Subramanyam Reddy, Swcnh/diamond-ethylene glycol nanofluid flow over a wedge, plate and stagnation point with induced magnetic field and nonlinear radiation – solar energy application, Eur. Phys. J. Spec. Top 228 (2019).

[19] K. Gelis, A. Naci Celik, K. Ozbek, O. Ozyurt, Experimental investigation into efficiency of sio2/water-based nanofluids in photovoltaic thermal systems using response surface methodology, Solar Energy 235 (2022) 229–241.

[20] T. Tayebi, A. Chamkha, Effects of various configurations of an inserted corrugated conductive cylinder on mhd natural convection in a hybrid nanofluid-filled square domain, J Therm Anal Calorim 143 (2021) 1399–1411.

[21] K. Thirumalaisamy, S. Ramachandran, V. Ramachandra Prasad, O. Anwar Bég, H.-H. Leung, F. Kamalov, K. Vajravelu, Comparative heat transfer analysis of γ- al2o3c2h6o2 and γ- al2o3h2o electroconductive nanofluids in a saturated porous square cavity with joule dissipation and heat source/sink effects, Physics of Fluids 34 (7) (2022) 072001.

[22] M. Hemmat Esfe, S. Esfandeh, S. Saedodin, H. Rostamian, Experimental evaluation, sensitivity analyzation and ann modeling of thermal conductivity of zno-mwcnt/eg-water hybrid nanofluid for engineering applications, Applied Thermal Engineering 125 (2017) 673–685.

[23] M. Sheikholeslami, S. Mehryan, A. Shafee, M. A. Sheremet, Variable magnetic forces impact on magnetizable hybrid nanofluid heat transfer through a circular cavity, Journal of Molecular Liquids 277 (2019) 388–396.

[24]M. Murugan, S. G., P. Muthukumar, C.-C. Wang, Role of hybrid-nanofluid in heat transfer enhancement – a review, International Communications in Heat and Mass Transfer 125 (2021).

[25]R. Sivaraj, S. Banerjee, Transport properties of non-newtonian nanofluids and applications, Eur. Phys. J. Spec. Top 230 (2021) 388–396.

[26]S. Hussain, K. Mehmood, M. Sagheer, A. Farooq, Entropy generation analysis of mixed convective flow in an inclined channel with cavity with al2o3-water nanofluid in porous medium, International Communications in Heat and Mass Transfer 89 (2017) 198–210.

[27]M. Siavashi, V. Bordbar, P. Rahnama, Heat transfer and entropy generation study of non-darcy double-diffusive natural convection in inclined porous enclosures with different source configurations, Applied Thermal Engineering 110 (2017) 1462–1475.

[28]R. Alluguvelli, C. S. Balla, K. Naikoti, O. D. Makinde, Nanofluid bioconvection in porous enclosure with viscous dissipation, Indian Journal of Pure Applied Physics 60 (2021) 78–89.

[29]E. S. Reddy, S. Panda, M. K. Nayak, O. D. Makinde, Cross flow on transient double-diffusive natural convection in inclined porous trapezoidal enclosures, Heat Transfer 50 (1) (2021) 849–875.

[30]E. Ushachew, M. Sharma, O. Makinde, Heat convection in micropolar nanofluid through porous medium-filled rectangular open enclosure: effect of an embedded heated object with different geometries, J Therm Anal Calorim 146 (2021) 1865–1881.

[31]M. Durairaj, S. Ramachandran, R. Mehdi, Heat generating/absorbing and chemically reacting casson fluid flow over a vertical cone and flat plate saturated with non-darcy porous medium, International Journal of Numerical Methods for Heat & Fluid Flow 27 (2017) 156–173.

[32]A. I. Alsabery, M. A. Ismael, A. J. Chamkha, I. Hashim, Effect of nonhomogeneous nanofluid model on transient natural convection in a non-darcy porous cavity containing an inner solid body, International Communications in Heat and Mass Transfer 110 (2020) 104442.

[33]Z. A. Raizah, A. M. Aly, S. E. Ahmed, Natural convection flow of a nanofluid-filled v-shaped cavity saturated with a heterogeneous porous medium: Incompressible smoothed particle hydrodynamics analysis, Ain Shams Engineering Journal 12 (2021) 2033–2046.

[34]N. Shirani, D. Toghraie, Numerical investigation of transient mixed convection of nanofluid in a cavity with non-darcy porous inner block and rotating cylinders with harmonic motion, Sci Rep 11 (2021) 17281.

[35]A. J. Ahrar, M. H. Djavareshkian, A. R. Ahrar, Numerical simulation of al2o3-water nanofluid heat transfer and entropy generation in a cavity using a novel tvd hybrid lb method under the influence of an external magnetic field source, Thermal Science and Engineering Progress 14 (2019) 100416.

[36]M. Muthtamilselvan, D. Doh, Magnetic field effect on mixed convection in a lid-driven square cavity filled with nanofluids, J Mech Sci Technol 28 (2014) 137–143.

[37]A. M. Rashad, A. J. Chamkha, M. A. Ismael, T. Salah, Magnetohydrodynamics natural convection in a triangular cavity filled with a cu-al2o3/water hybrid nanofluid with localized heating from below and internal heat generation, ASME. J. Heat Transfer 140 (2018) 072502.

[38]R. Du, P. Gokulavani, M. Muthtamilselvan, F. Al-Amri, B. Abdalla, Influence of the lorentz force on the ventilation cavity having a centrally placed heated baffle filled with the *cual*2*o*3*h*2*o* hybrid nanofluid, International Communications in Heat and Mass Transfer 116 (2020) 104676.

[39]G. Sowmya, B. Gireesha, A. I. et al., Significance of buoyancy and lorentz forces on water-conveying iron(iii) oxide and silver nanoparticles in a rectangular cavity mounted with two heated fins: heat transfer analysis, J Therm Anal Calorim 144 (2021) 2369–2384.

[40]A. T. Mohamed, W. M. El-Maghlany, Augmentation of natural convective heat transfer in square cavity by utilizing nanofluids in the presence of magnetic field and uniform heat generation/absorption, International Journal of Thermal Sciences 58 (2012) 130–142.

[41]B. Mliki, M. A. Abbassi, A. Omri, B. Zeghmati, Augmentation of natural convective heat transfer in linearly heated cavity by utilizing nanofluids in the presence of magnetic field and uniform heat generation/absorption, Powder Technology 284 (2015) 312–325.

[42]S. Hussain, H. F. Öztop, K. Mehmood, N. Abu-Hamdeh, Effects of inclined magnetic field on mixed convection in a nanofluid filled double lid-driven cavity with volumetric heat generation or absorption using finite element method, Chinese Journal of Physics 56 (2018) 484–501.

[43]A. Abdulkadhim, H. K. Hamzah, F. H. Ali, Çağatay Yıldız, A. M. Abed, E. M. Abed, M. Arıcı, Effect of heat generation and heat absorption on natural convection of cu-water nanofluid in a wavy enclosure under magnetic field, International Communications in Heat and Mass Transfer 120 (2021) 105024.

[44]C. Christov, On frame indifferent formulation of the maxwell–cattaneo model of finite-speed heat conduction, Mechanics Research Communications 36 (2009) 481–486.

[45]N. Muhammad, S. Nadeem, A. Issakhov, Finite volume method for mixed convection flow of ag–ethylene glycol nanofluid flow in a cavity having thin central heater, Physica A: Statistical Mechanics and its Applications 537 (2020) 122738.

[46]S. Jakeer, P. BalaAnki Reddy, A. Rashad, H. A. Nabwey, Impact of heated obstacle position on magneto-hybrid nanofluid flow in a lid-driven porous cavity with cattaneo-christov heat flux pattern, Alexandria Engineering Journal 60 (2021) 821–835.

[47]S. Sivasankaran, M. Bhuvaneswari, A. Amer, Numerical study on buoyant convection and thermal radiation in a cavity with various thermal sources and cattaneo-christov heat flux, Case Studies in Thermal Engineering 27 (2021) 101207.

[48]R. Garia, S. K. Rawat, M. Kumar, M. Yaseen, Hybrid nanofluid flow over two different geometries with cattaneo–christov heat flux model and heat generation: A model with correlation coefficient and probable error, Chinese Journal of Physics 74 (2021) 421–439.

[49]O. Anwar Bég, K. Venkatadri, V. Ramachandra Prasad, T. Bég, A. Kadir, H. J. Leonard, Numerical simulation of hydromagnetic marangoni convection flow in a darcian porous semiconductor melt enclosure with buoyancy and heat generation effects, Materials Science and Engineering: B 261 (2020) 114722.

[50]B. H. Khan, V. R. Prasad, R. B. Vijaya, Thermal radiation on mixed convective flow in a porous cavity: Numerical simulation, Nonlinear Engineering 7 (2018) 253–261.

[51]R. Sivaraj, B. Rushi Kumar, Viscoelastic fluid flow over a moving vertical cone and flat plate with variable electric conductivity, International Journal of Heat and Mass Transfer 61 (2013) 119–128.

[52]M. Mansour, S. Siddiqa, R. S. R. Gorla, A. Rashad, Effects of heat source and sink on entropy generation and mhd natural convection of al2o3-cu/water hybrid nanofluid filled with square porous cavity, Thermal Science and Engineering Progress 6 (2018) 57–71.

[53]W. Al-Kouz, A. Abderrahmane, e. a. Shamshuddin, M., Heat transfer and entropy generation analysis of water-fe3o4/cnt hybrid magnetic nanofluid flow in a trapezoidal wavy enclosure containing porous media with the galerkin finite element method, Eur. Phys. J. Plus 136 (2021) 1184.

[54]T. Islam, M. Alam, M. e. a. Asjad, Heatline visualization of mhd natural convection heat transfer of nanofluid in a prismatic enclosure, Sci Rep 11 (2021) 10972.

[55]S. Khalid, I. Zakaria, A. W. et al., Thermal–electrical–hydraulic properties of al2o3–sio2 hybrid nanofluids for advanced pem fuel cell thermal management, J Therm Anal Calorim 143 (2021) 1555–1567.

[56]F. Harlow, J. Welch, Numerical calculation of time dependent viscous incompressible flow of fluid with free surface, Physics of Fluids 8 (1965) 2182–2189.

[57]R. U. Urunkar, S. D. Patil, Enhancement of heat and mass transfer characteristics of metal hydride reactor for hydrogen storage using various nanofluids, International Journal of Hydrogen Energy 46 (2021) 19486–19497.

[58]W. L. A. Vielstich, H. Gasteiger, Handbook of fuel cells. fundamentals, technology, applications (2003).

Figure I

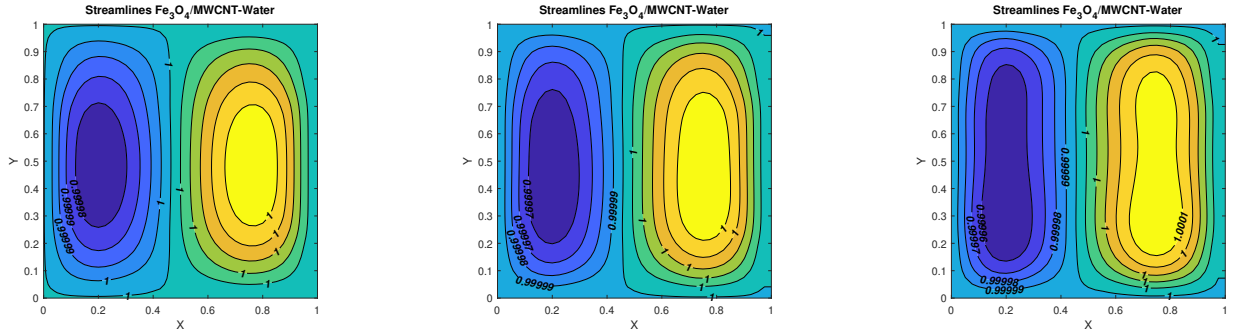

Figure II

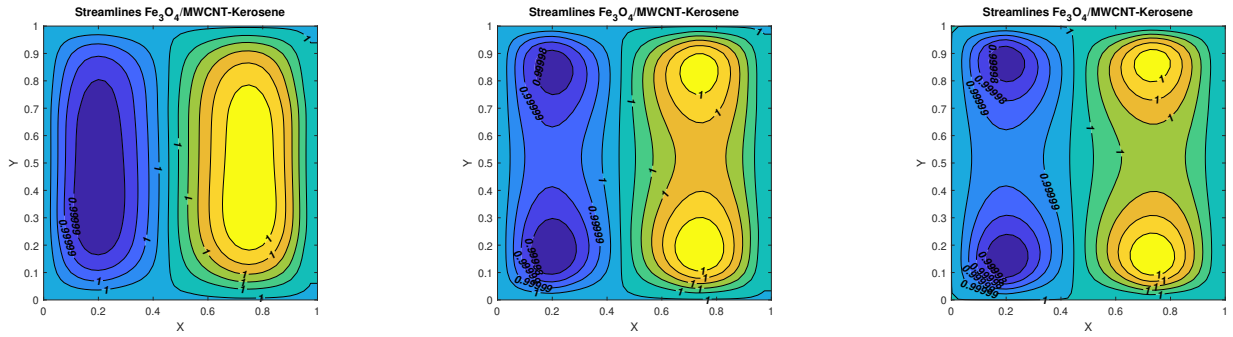

FIG. 4. Streamlines of (I) $Fe_3O_4 - MWCNT$ −water and (II) $Fe_3O_4 - MWCNT$ −kerosene for distinct values of (A) $Re = 1$, (B) $Re = 3$, (C) $Re = 5$.

Figure I

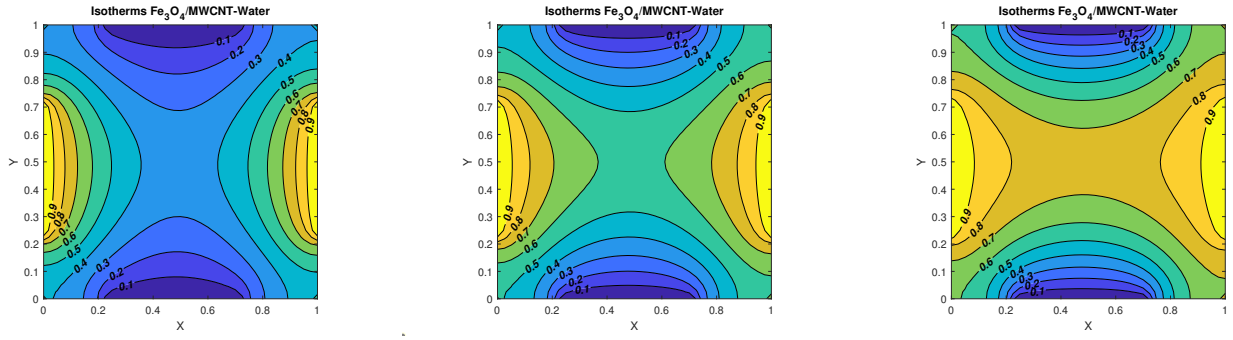

Figure II

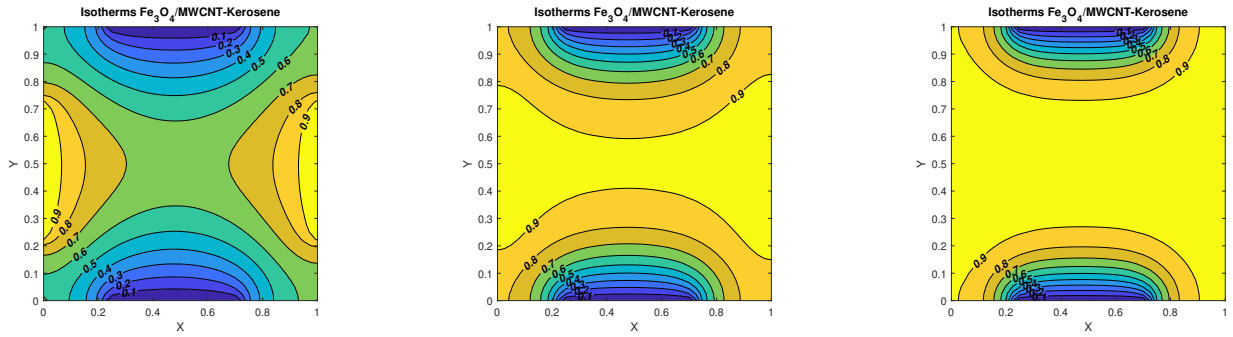

FIG. 5. Isotherms of (I) $Fe_3O_4 - MWCNT$ −water and (II) $Fe_3O_4 - MWCNT$ −kerosene for distinct values of (A) $Re = 1$, (B) $Re = 3$, (C) $Re = 5$.

Figure I

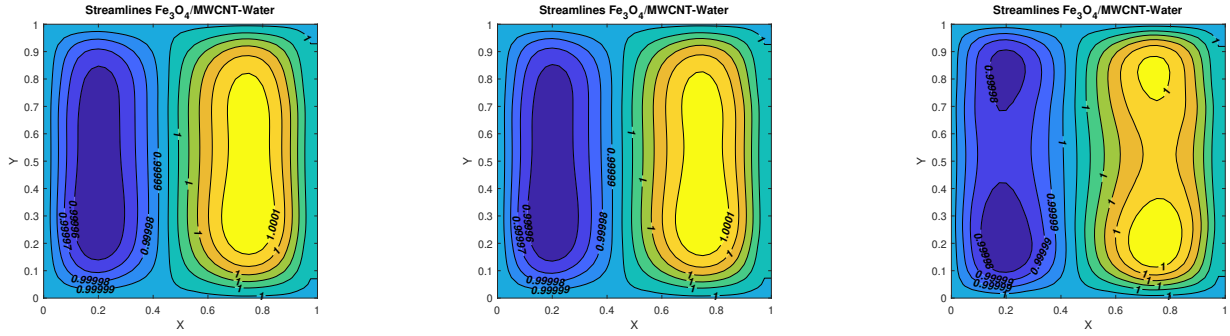

Figure II

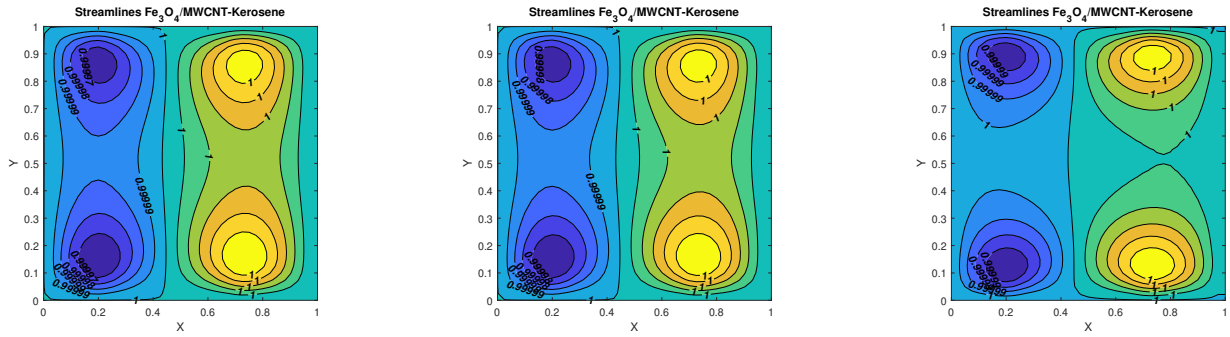

FIG. 6. Streamlines of (I) $Fe_3O_4 - MWCNT-$water and (II) $Fe_3O_4 - MWCNT-$kerosene for distinct values of (A) $Ha = 0$, (B) $Ha = 10$, (C) $Ha = 50$.

Figure I

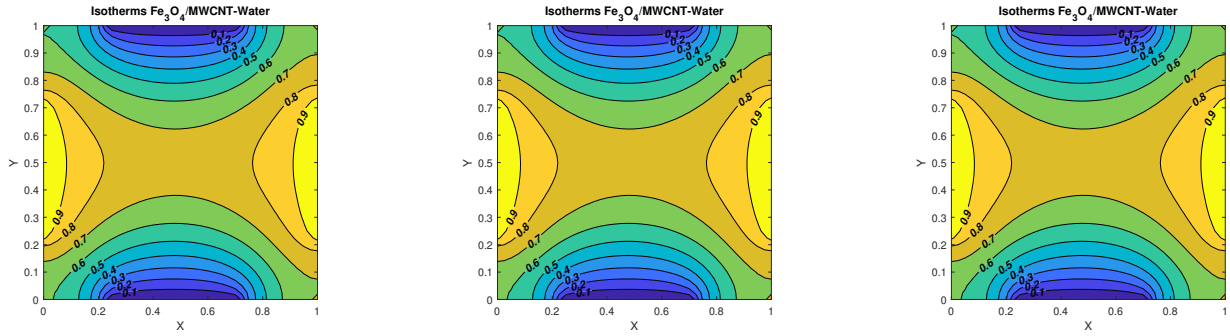

Figure II

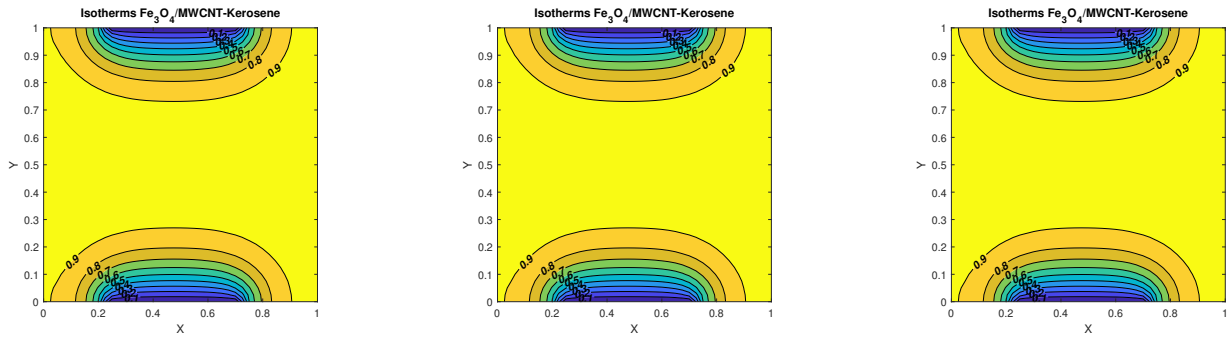

FIG. 7. Isotherm of $(I)Fe_3O_4 - MWCNT-$ water and $(II)Fe_3O_4 - MWCNT-$kerosene for distinct values of (A) $Ha = 0$, (B) $Ha = 10$, (C) $Ha = 50$.

Figure I

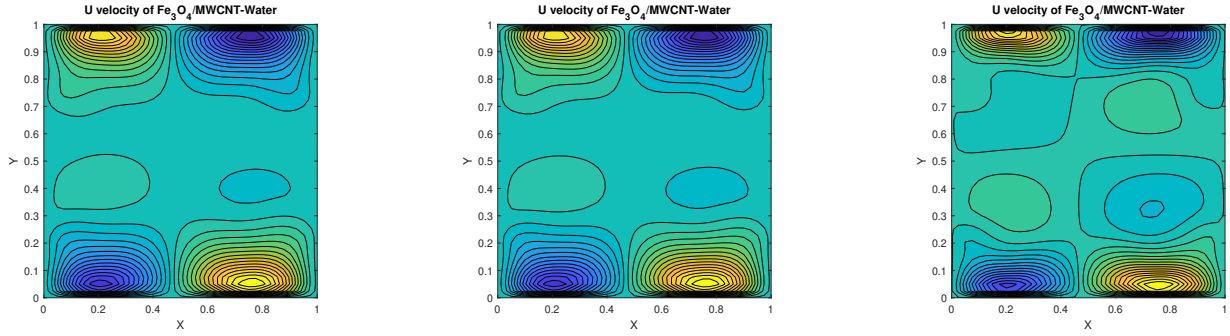

Figure II

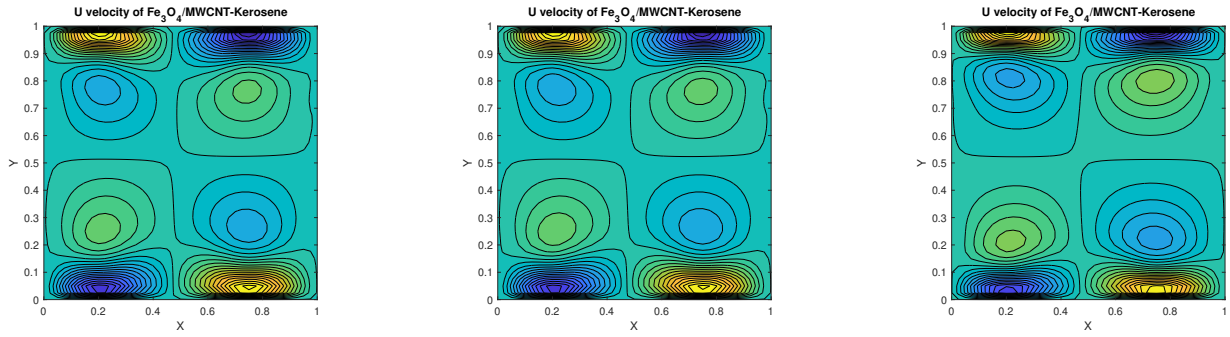

FIG. 8. U velocity of (I) $Fe_3O_4 - MWCNT-$water and (II) $Fe_3O_4 - MWCNT-$kerosene for distinct values of (A) $Ha = 0$, (B) $Ha = 10$, (C) $Ha = 50$.

Figure I

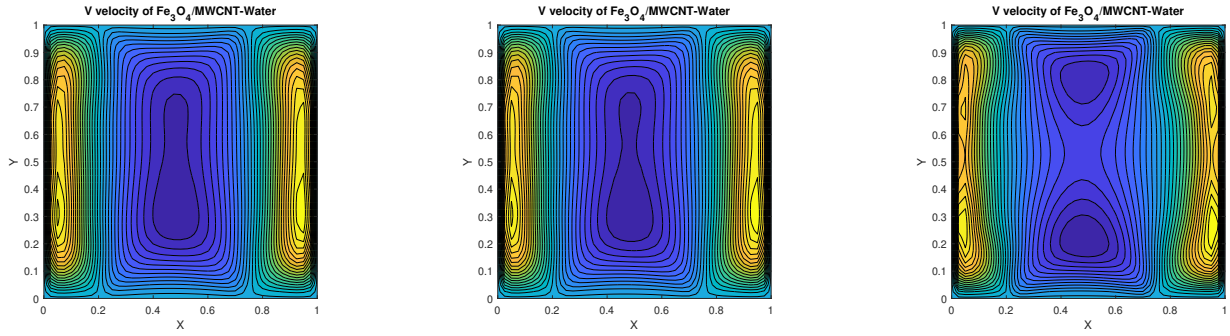

Figure II

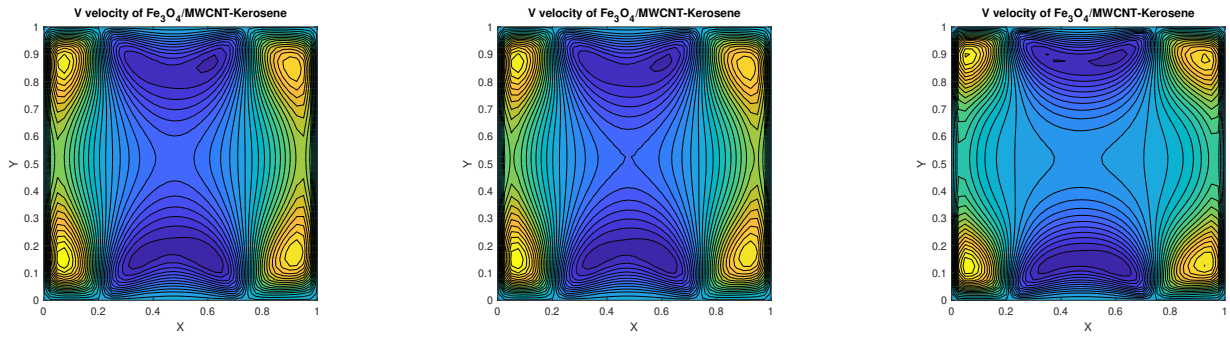

FIG. 9. V velocity of (I) $Fe_3O_4 - MWCNT-$water and (II) $Fe_3O_4 - MWCNT-$kerosene for distinct values of (A) $Ha = 0$, (B) $Ha = 10$, (C) $Ha = 50$.

Figure I

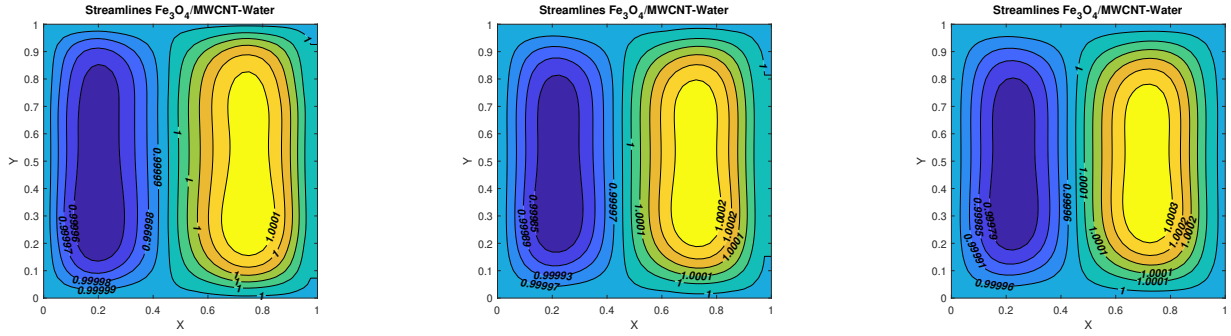

Figure II

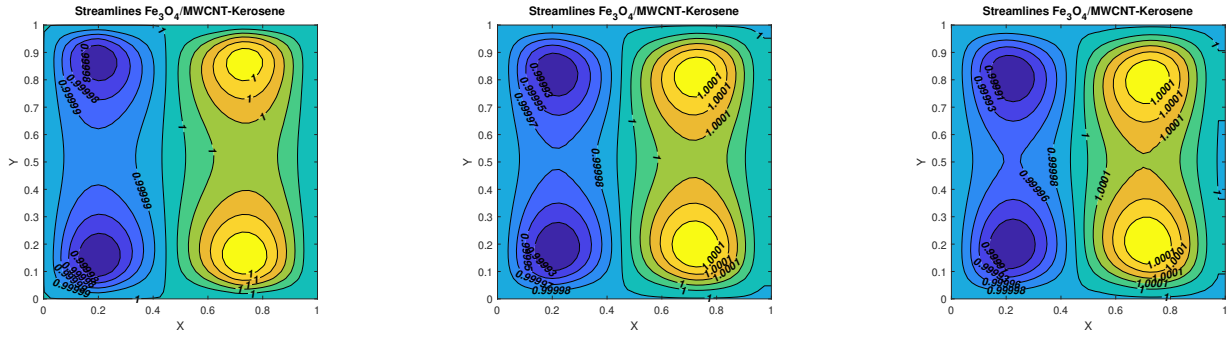

FIG. 10. Streamlines of (I) $Fe_3O_4 - MWCNT -$water and (II) $Fe_3O_4 - MWCNT -$kerosene for distinct values of (A) $Da = 10^{-3}$, (B) $Da = 10^{-2}$, (C) $Da = 10^{-1}$.

Figure I

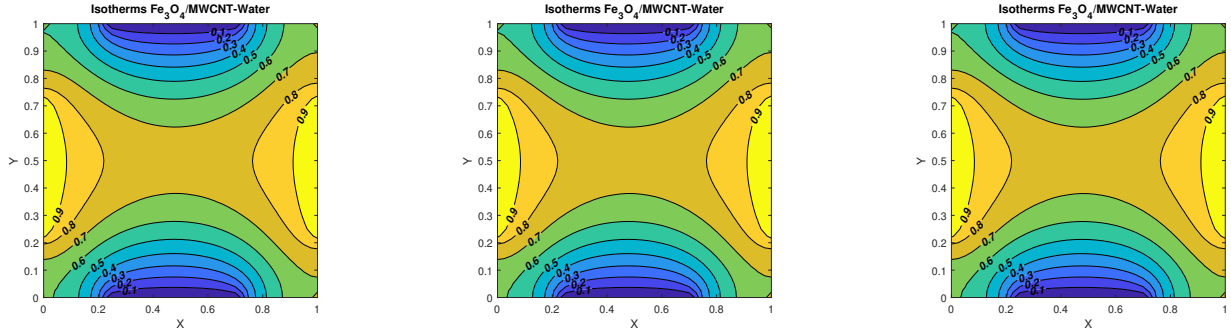

Figure II

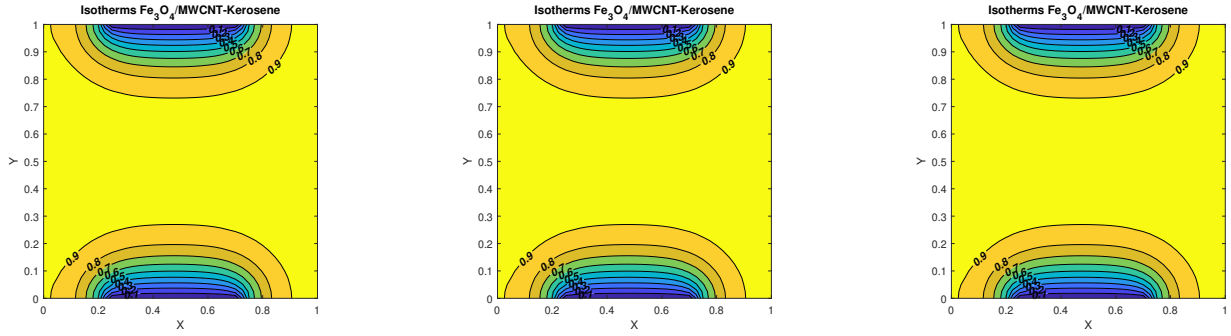

FIG. 11. Isotherms of (I) $Fe_3O_4 - MWCNT -$water and (II) $Fe_3O_4 - MWCNT -$kerosene for distinct values of (A) $Da = 10^{-3}$, (B) $Da = 10^{-2}$, (C) $Da = 10^{-1}$.

Figure I

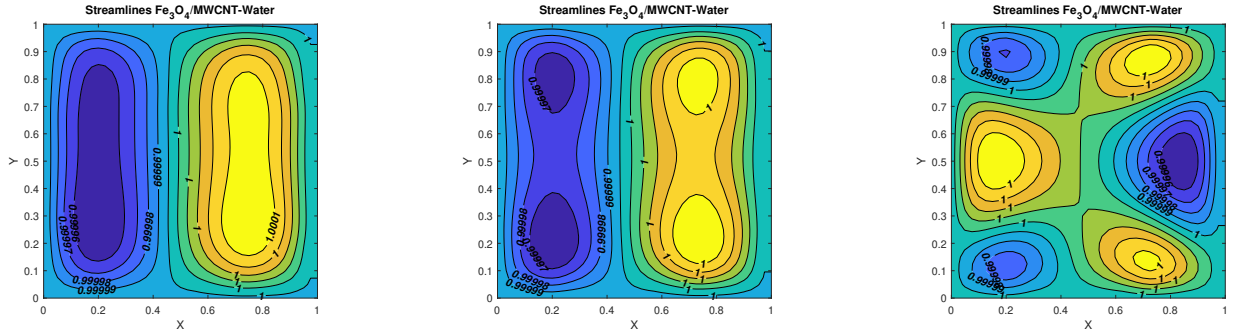

Figure II

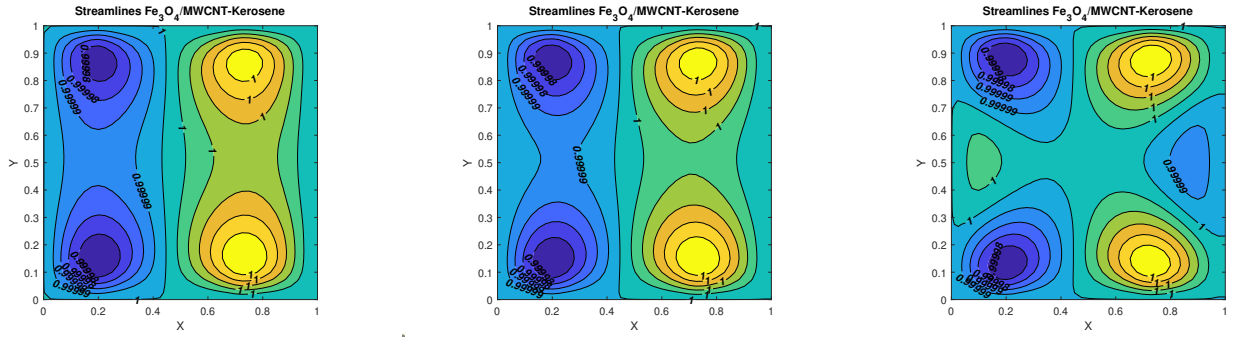

FIG. 12. Streamlines of (I) $Fe_3O_4 - MWCNT -$water and (II) $Fe_3O_4 - MWCNT -$kerosene for distinct values of (A) $Q = -5$, (B) $Q = 0$, (C) $Q = 15$.

Figure I

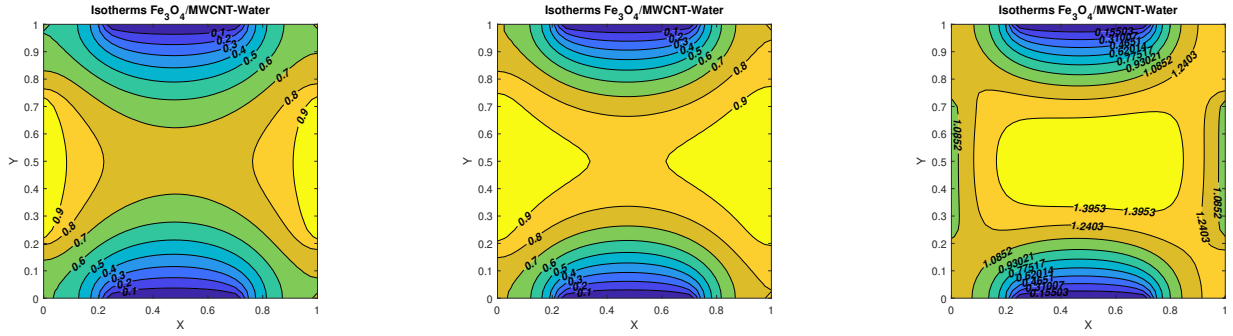

Figure II

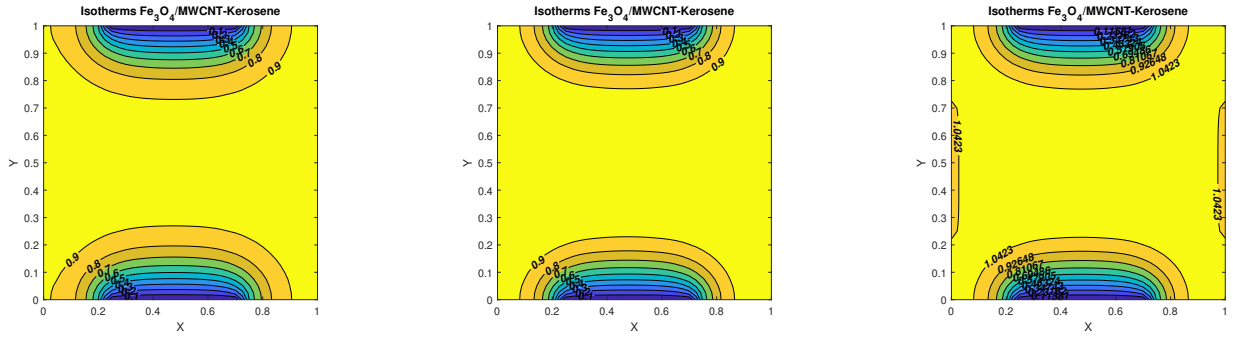

FIG. 13. Isotherms of (I) $Fe_3O_4 - MWCNT -$water and (II) $Fe_3O_4 - MWCNT -$kerosene for distinct values of (A) $Q = -5$, (B) $Q = 0$, (C) $Q = 15$.

Figure I

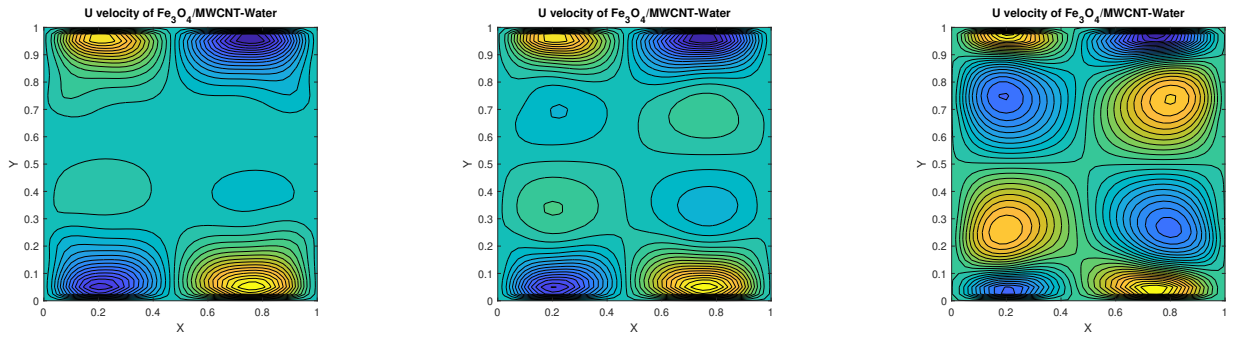

Figure II

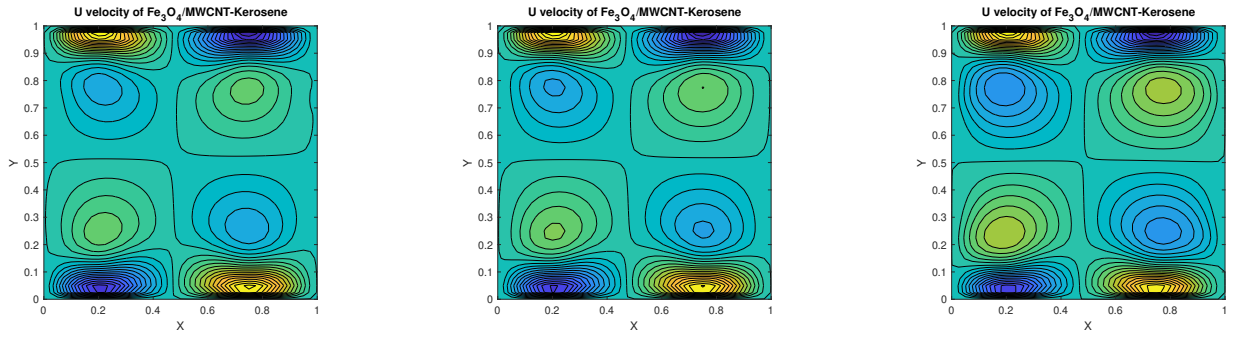

FIG. 14. U velocity of (I) $Fe_3O_4 - MWCNT$ −water and (II) $Fe_3O_4 - MWCNT$ −kerosene for distinct values of (A) $Q = -5$, (B) $Q = 0$, (C) $Q = 15$.

Figure I

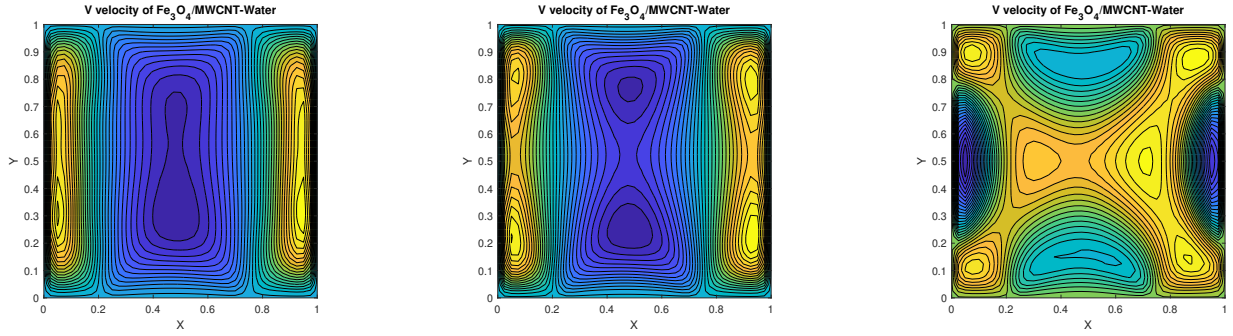

Figure II

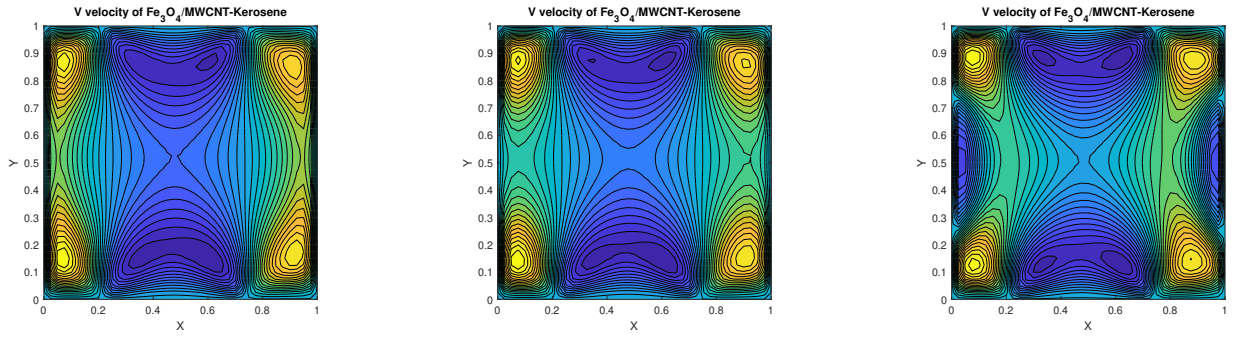

FIG. 15. V velocity of (I) $Fe_3O_4 - MWCNT$ −water and (II) $Fe_3O_4 - MWCNT$ −kerosene for distinct values of (A) $Q = -5$, (B) $Q = 0$, (C) $Q = 15$.

Figure I

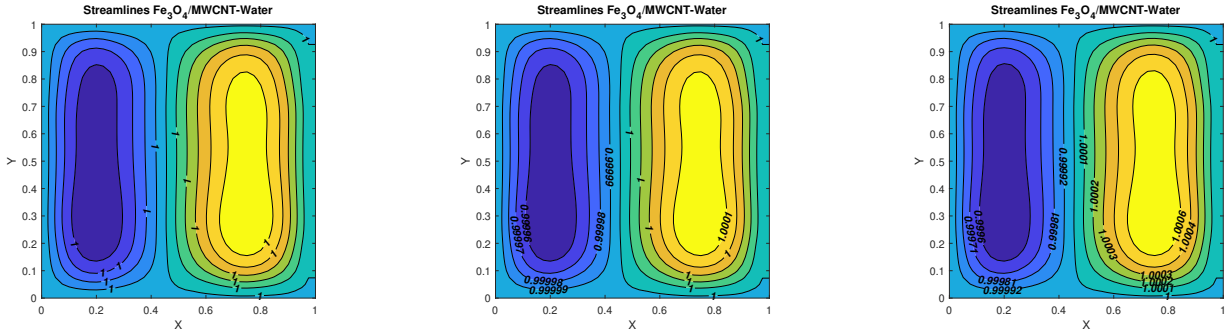

Figure II

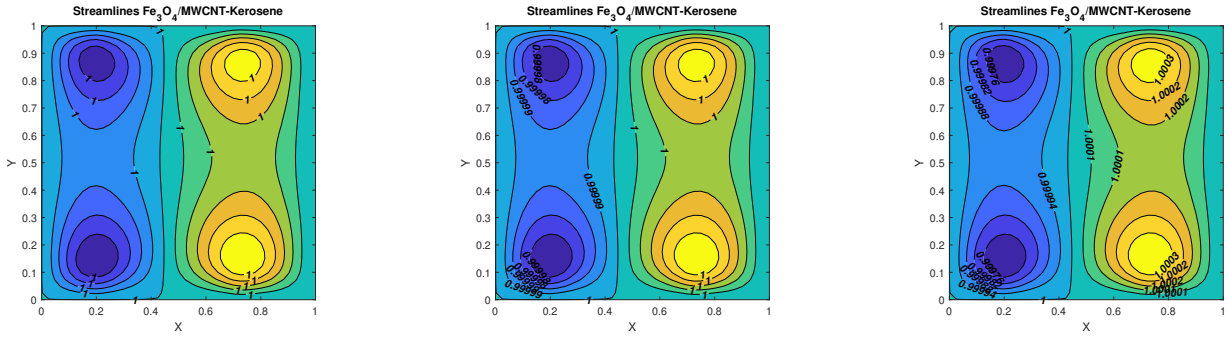

FIG. 16. Streamlines of (I) $Fe_3O_4 - MWCNT -$water and (II) $Fe_3O_4 - MWCNT -$kerosene for distinct values of (A) $Ri = 0.01$, (B) $Ri = 1$, (C) $Ri = 10$.

Figure I

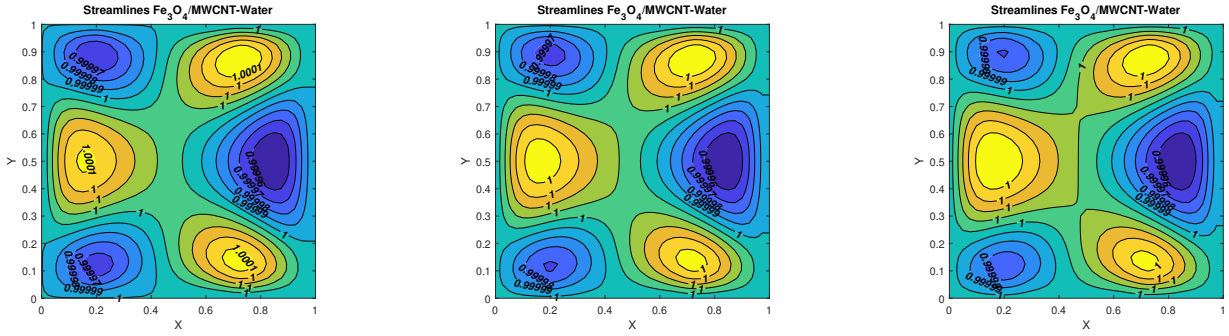

Figure II

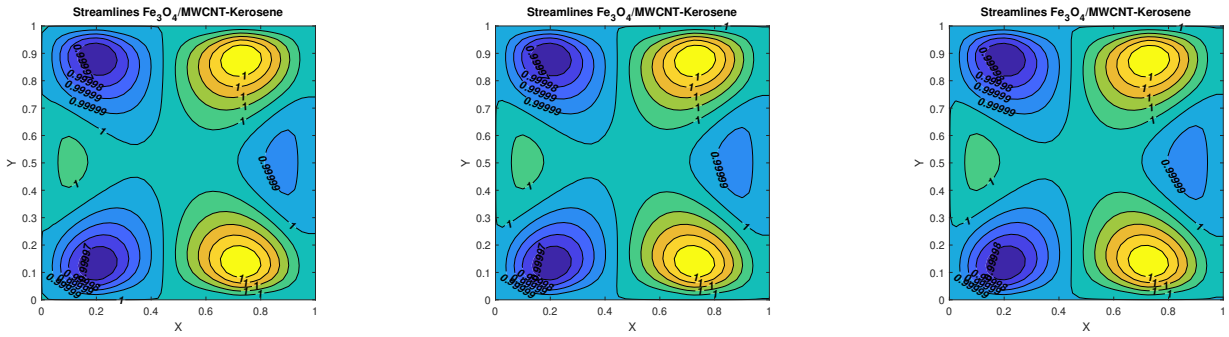

FIG. 17. Streamlines of (I) $Fe_3O_4 - MWCNT -$water and (II) $Fe_3O_4 - MWCNT -$kerosene for distinct values of (A) $\Phi = 1\%$, (B) $\Phi = 3\%$, (C) $\Phi = 5\%$.

Figure I

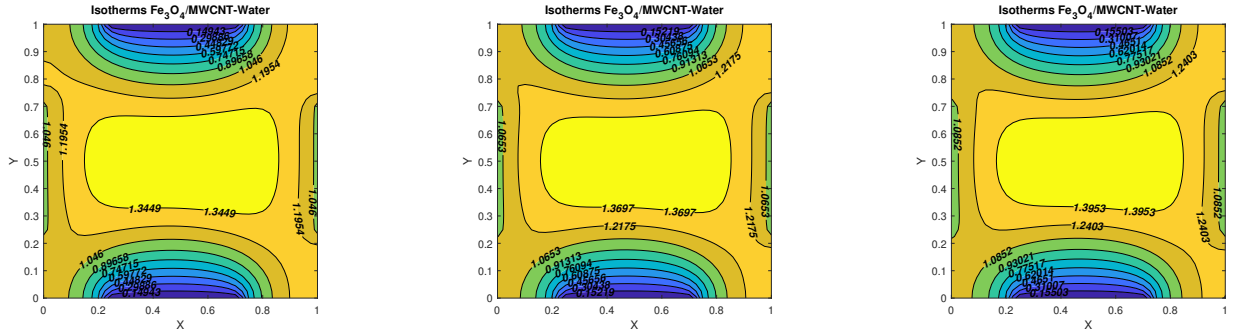

Figure II

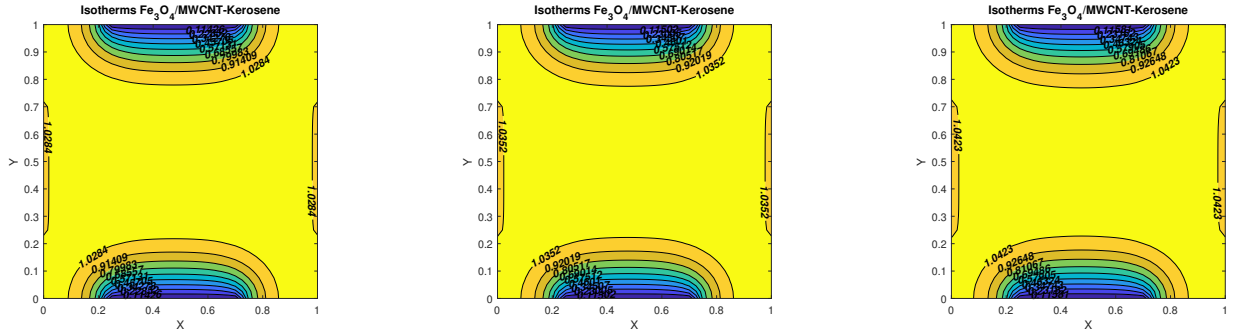

FIG. 18. Isotherms of (I) $Fe_3O_4 - MWCNT$ −water and (II) $Fe_3O_4 - MWCNT$ −kerosene for distinct values of (A) $\Phi = 1\%$, (B) $\Phi = 3\%$, (C) $\Phi = 5\%$.

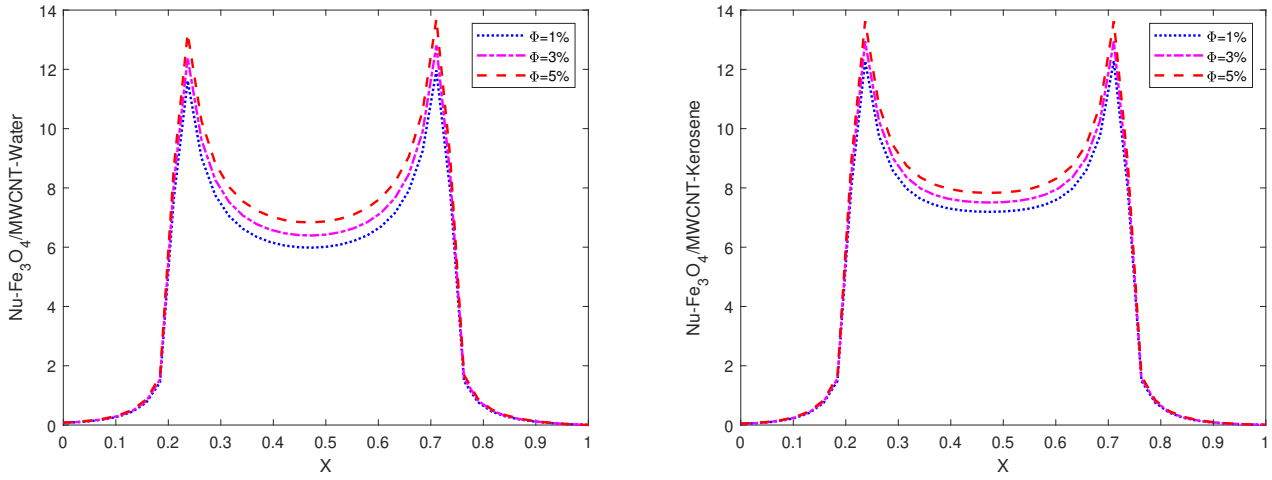

FIG. 19. Local Nusselt number of (I) $Fe_3O_4 - MWCNT$ −water and (II) $Fe_3O_4 - MWCNT$ −kerosene hybrid nanofluids.

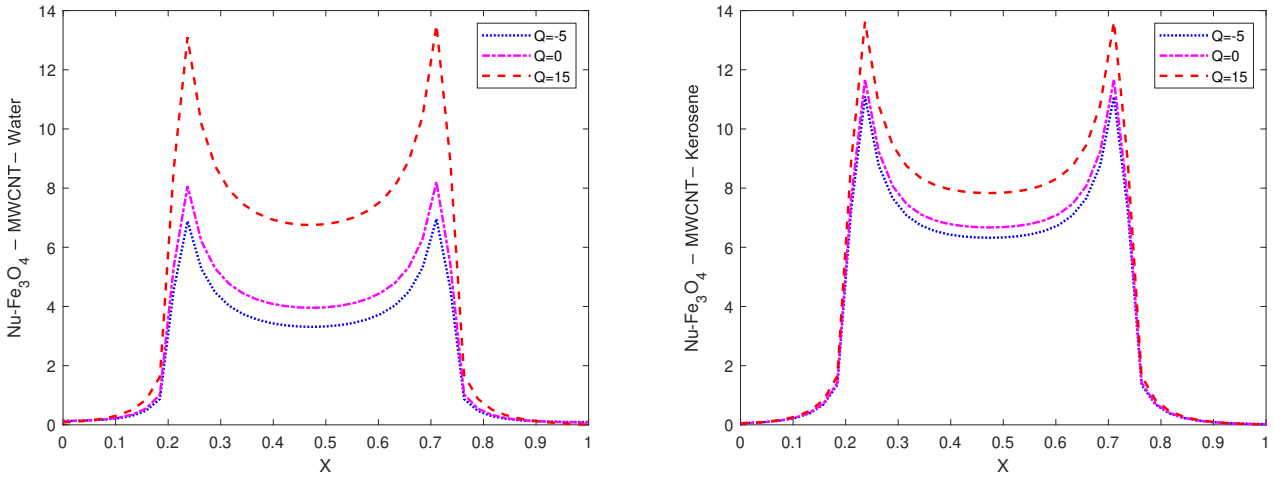

FIG. 20. Local Nusselt number of (I) $Fe_3O_4 - MWCNT -$ water and (II) $Fe_3O_4 - MWCNT -$kerosene hybrid nanofluids.

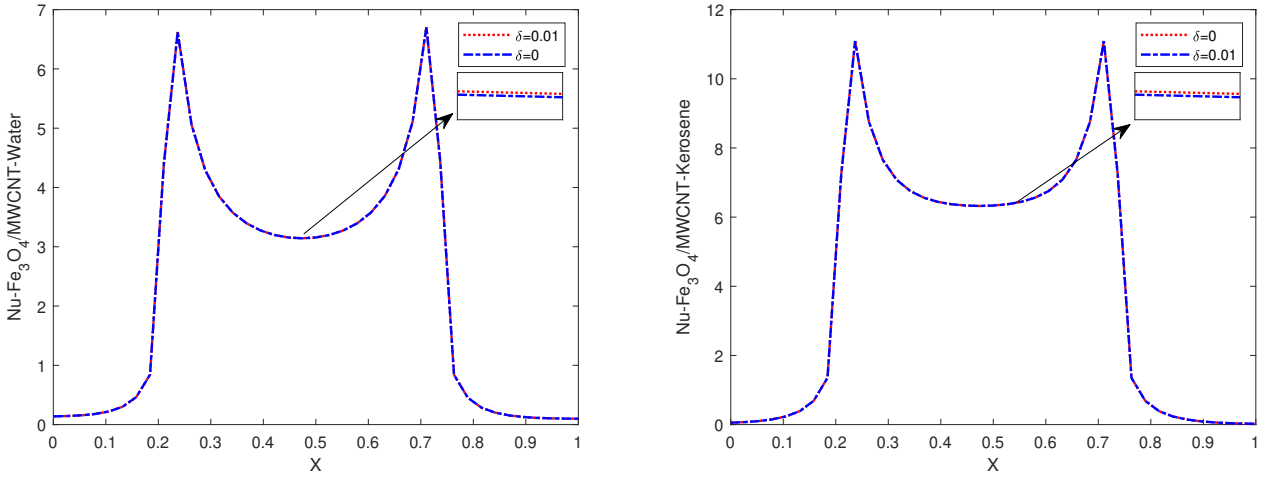

FIG. 21. Local Nusselt number of (I) $Fe_3O_4 - MWCNT -$water and (II) $Fe_3O_4 - MWCNT -$kerosene hybrid nanofluids.